Chapter 4

SEMI-EMPIRICAL TYRE MODELS

4.1. Introduction

In the preceding chapter the theory of the tyre force and moment generating properties have been dealt with based on physical tyre models. The present chapter treats models that have been specifically designed to represent the tyre as a vehicle component in a vehicle simulation environment. The modelling approach is termed 'semi-empirical' because the models are based on measured data but may contain structures that find their origin in physical models like those treated in the preceding chapter. The mathematical descriptions are restricted to steady-state situations. The non-steady-state behaviour will be discussed in subsequent chapters.

In the past, several types of mathematical functions have been used to describe the cornering force characteristic. Exponential, arctangent, parabolic (up to its maximum) and hyperbolic tangent functions (difference of two) have been tried with more and less success. Often, only very crude approximations could be achieved. To improve the accuracy, tables of measured data points have been used together with interpolation schemes. Also, higher order polynomials were popular but proved not always suitable in terms of accuracy and the very large deviations that occur outside the ranges of slip covered by the original measurement data used in the fitting process. Mathematical representations of longitudinal force and aligning torque came later and only relatively recently the combined slip condition was included in the empirical description. The longitudinal slip ratio was introduced as an input variable instead of the braking or driving force which was common practice in the early days of vehicle dynamics analysis. This latter method, however, is still in use for certain applications.

In the following sections of this chapter, first, a relatively simple approach will be discussed that is based on the similarity concept and after that, in the remainder of the chapter, a detailed description will be given of the *Magic Formula* tyre model. The two model approaches belong to the second and first categories of Fig.2.11 respectively.

4.2. The Similarity Method

The method to be discussed in this section is based on the observation that the pure slip curves remain approximately similar in shape when the tyre runs at conditions that are different from the reference condition. The reference condition is defined here as the state where the tyre runs at its rated (nominal) load (F_{zo}), at camber equal to zero ($\gamma = 0$), at either free rolling ($\kappa = 0$) or at side slip equal to zero ($\alpha = 0$) and on a given road surface (μ_o). A similar shape means that the characteristic that belongs to the reference condition is regained by vertical and horizontal multiplications and shifting of the curve. The similarity method has been first used by Pacejka (1958) and later by Radt and Pacejka (1963). A demonstration that in practice similarity indeed approximately occurs is given by Radt and Milliken (1983), also see Milliken and Milliken (1995). The Figs.4.1 and 4.2 present the results when the force and moment as well as the slip angle have been normalised resulting in the non-dimensional quantities shown along the axes. The raw data have been processed to make the characteristics pass through the origin of the graph. The curve results from a Magic Formula fit. The parameters B', C', D' and E' for the non-dimensional
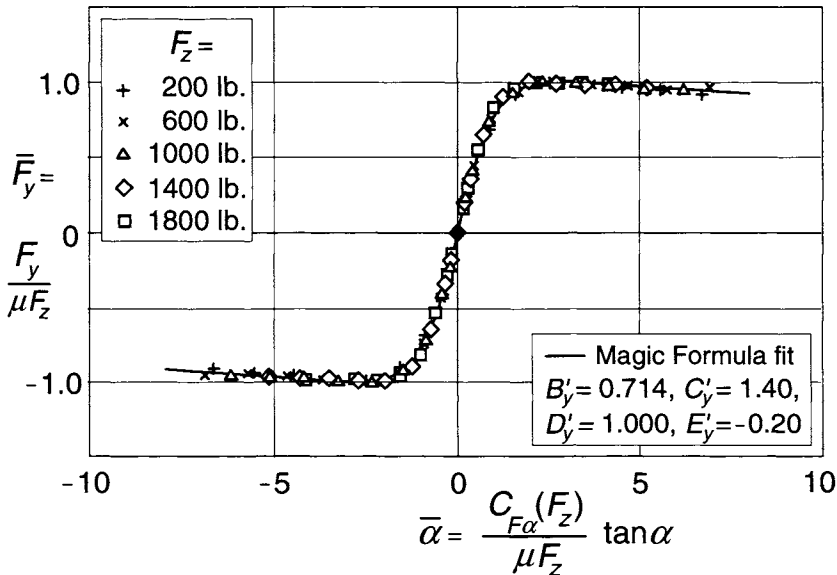

Fig. 4.1. Result of Radt's non-dimensionalisation of tyre characteristics showing that the tyre side force characteristics measured at different loads reduce to virtually the same curve when the force and the slip angle are normalised as indicated.
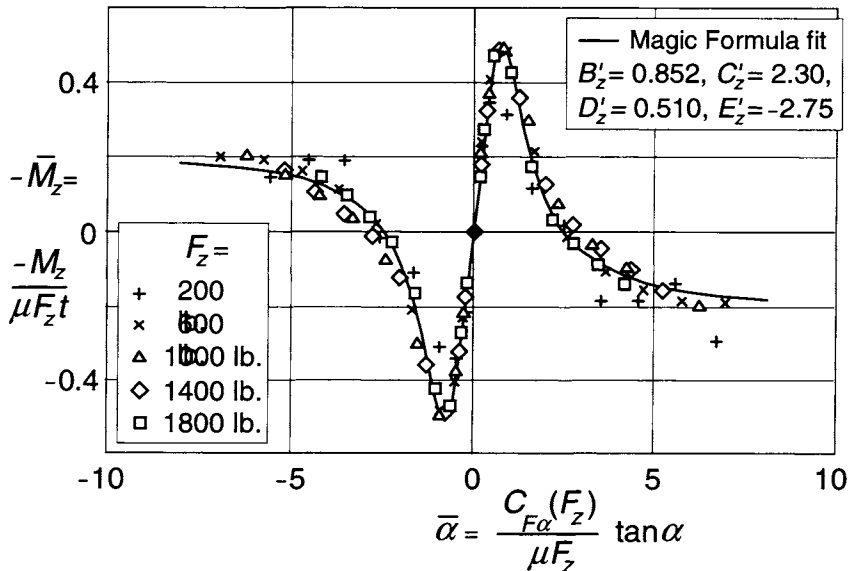
Fig. 4.2. Result of Radt's non-dimensionalisation of the tyre aligning torque characteristic after normalising the moment and the slip angle as indicated; t represents the pneumatic trail at vanishing slip angle.

side force (subscript $_y$) and for the non-dimensional moment (subscript $_z$) have been used in the non-dimensional version of the Magic Formula given in Eqs.(1.6) and similar for the moment. Later on, the formula will be introduced again, Eqs.(4.6,4.10).

The resulting model is through its simplicity relatively fast. It is capable to represent pure slip conditions rather well including the influence of a camber angle. The description of the situation at combined lateral and longitudinal slip is qualitatively satisfactory. Quantitatively, however, deviations may occur at higher levels of the combined two slip values.

4.2.1. Pure Slip Conditions

The functions representing the reference curves which are found at pure slip conditions are designated with the subscript $_o$. We have, for instance, the reference function $F_y = F_{yo}(\alpha)$ that represents the side force vs slip angle relationship at nominal load F_{zo}, with longitudinal slip and camber equal to zero and the friction level represented by μ_o. We may now try to change the condition to a situation at a different wheel load F_z. Two basic changes will occur with the characteristic: (1) a change in level of the curve where saturation of the side

force takes place (peak level) and (2) a change in slope at vanishing side slip ($\alpha = 0$). The first modification can be created by multiplying the characteristic both in vertical and horizontal direction with the ratio F_z / F_{zo}. The horizontal multiplication is needed to not disturb the original slope. We obtain for the new function:

$$F_y = \frac{F_z}{F_{zo}} F_{yo}(\alpha_{eq}) \tag{4.1}$$

with the equivalent slip angle:

$$\alpha_{eq} = \frac{F_{zo}}{F_z} \alpha \tag{4.2}$$

Because, obviously, the derivative of F_{yo} with respect to its argument α_{eq} at $\alpha_{eq} = 0$ is equal to the original cornering stiffness $C_{F\alpha o}$, we find for the derivative of F_y with respect to α the same value for the slope at $\alpha = 0$:

$$\frac{\partial F_y}{\partial \alpha} = \frac{F_z}{F_{zo}} \frac{dF_{yo}}{d\alpha_{eq}} \frac{\partial \alpha_{eq}}{\partial \alpha} = \frac{dF_{yo}}{d\alpha_{eq}} = C_{F\alpha o} \tag{4.3}$$

which proves that the slope at the origin of the characteristic is not affected by the successive multiplications. The second step in the manipulation of the
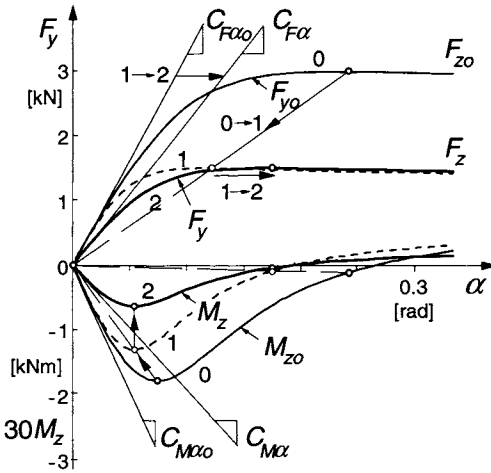

Fig. 4.3. Using the similarity method to adapt F_y and M_z curves to a new level of load.
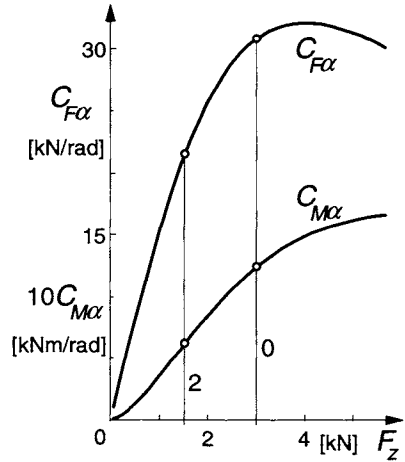
Fig. 4.4. Cornering and aligning stiffness vs wheel load.

original curve is the adaptation of the slope. This is accomplished by a horizontal multiplication of the newly obtained characteristic. This is done by multiplying the argument with the ratio of the new and the original cornering stiffness. Consequently, the new argument reads:

$$\alpha_{eq} = \frac{C_{F\alpha}(F_z)}{C_{F\alpha o}} \frac{F_{zo}}{F_z} \alpha \qquad (4.4)$$

Together with Eq.(4.1) we have the new formulation for the side force vs slip angle relationship at the new load F_z. In Fig.4.3 the two steps taken to obtain the new curve have been illustrated. Here, the nominal load $F_{zo} = 3000$N and the new load $F_z = 1500$N.

In the same figure the characteristic of the aligning torque has been adapted to the new condition. For this, we use the knowledge gained when working with the brush model (cf. Fig.3.4). More specifically, we will obey the rule that according to the theory, obviously, the point where the M_z curve reaches the α axis lies below the peak of the F_y curve. In Fig.3.4 this occurs at $\tan\alpha = 1/\theta_y$. This requirement means that the same equivalent slip angle (4.4) must be used as for the argument of the F_y function (4.1). Secondly, we will use information on the new value of the aligning stiffness $C_{M\alpha}$. The reference curve for M_{zo} that is used is more realistic than the theoretical curve of Fig.3.4. Typically, the moment changes its sign in the larger slip angle range where F_y reaches its peak.

With the same equivalent slip angle and the new aligning stiffness we obtain the expression for the new value of the aligning torque according to the similarity concept:

$$M_z = \frac{F_z}{F_{zo}} \frac{C_{M\alpha}(F_z)}{C_{M\alpha o}} \frac{C_{F\alpha o}}{C_{F\alpha}(F_z)} M_{zo}(\alpha_{eq}) \qquad (4.5)$$

The first and third factors being the inverse of the multiplication factor used in (4.4), are needed to maintain the original slope. The second factor multiplies the intermediate M_z curve (1 in Fig.4.3) in vertical direction to adapt the slope to its new value (2) while not disturbing the α scale. It may be noted that the combined second and third factor equals the ratio of the new and the original values of the pneumatic trail t/t_o.

For the calculations connected with Fig.4.3 the reference characteristics for F_{yo}, M_{zo} and $C_{F\alpha}$ have been described by means of the *Magic Formula* type functions (cf. Eqs.(1.6)). For this occasion, the aligning stiffness is modelled as the product of a certain fraction of the contact length $2a$ and the cornering stiffness. The resulting characteristics for these four quantities as shown in Figs. 4.3 and 4.4 are realistic. The following formulae have been used:

Side force at nominal load F_{zo}

$$F_{yo} = D_{yo} \sin[C_y \arctan\{B_{yo}\alpha - E_y(B_{yo}\alpha - \arctan(B_{yo}\alpha))\}] \qquad (4.6)$$

with stiffness factor

$$B_{yo} = C_{Fao}/(C_y D_{yo}) \qquad (4.7)$$

peak factor for the side force which in general is different from the one for the longitudinal force, consequently we introduce μ_{yo} beside μ_{xo}:

$$D_{yo} = \mu_{yo} F_{zo} \qquad (4.8)$$

and cornering stiffness as function of wheel load F_z

$$C_{Fa} = c_1 c_2 F_{zo} \sin\left\{2 \arctan\left(\frac{F_z}{c_2 F_{zo}}\right)\right\} \qquad (4.9)$$

Aligning torque at nominal wheel load:

$$M_{zo} = D_{zo} \sin[C_z \arctan\{B_{zo}\alpha - E_z(B_{zo}\alpha - \arctan(B_{zo}\alpha))\}] \qquad (4.10)$$

with stiffness factor

$$B_{zo} = -C_{Mao}/(C_z D_{zo}) \qquad (4.11)$$

peak factor (a_o representing half the contact length at nominal load)

$$D_{zo} = c_3 a_o D_{yo} \qquad (4.12)$$

and aligning stiffness as function of wheel load F_z

$$C_{Ma} = t C_{Fa} = c_4 a C_{Fa} \qquad (4.13)$$

where apparently the pneumatic trail $t=c_4 a$. Half the contact length a is assumed to be proportional with the square root of the wheel load

$$a = a_o \sqrt{F_z/F_{zo}} \qquad (4.14)$$

The resulting approximation of the pneumatic trail turns out to be quite adequate and might be considered to be used in the set of Magic Formula Tyre model equations (4.E42) to be dealt with later on.

The values of parameters used for the calculations to be conducted have been listed in Table 4.1.

Table 4.1. Parameter values used in Section 4.2

F_{zo}	3000 N	C_y	1.3	C_x	1.5	c_1	8	c_5	1	c_9	0.3
a_o	0.08 m	E_y	−1	E_x	−1	c_2	1.33	c_6	0.3	c_{10}	0
b	0.07 m	C_z	2.3	μ_{yo}	1	c_3	0.25	c_7	100	c_{11}	4
r_e	0.30 m	E_z	-2	μ_{xo}	1.26	c_4	0.5	c_8	15		

The next two items we will deal with are a change in friction coefficient from μ_{yo} to μ_y and the introduction of a camber angle γ. The first change can be handled by multiplying the curves in radial direction with factor μ_y/μ_{yo}. Together with the change in load we find:

$$F_y = \frac{\mu_y F_z}{\mu_{yo} F_{zo}} F_{yo}(\alpha_{eq}) \tag{4.15}$$

with

$$\alpha_{eq} = \frac{C_{F\alpha}(F_z)}{C_{F\alpha o}} \frac{\mu_{yo} F_{zo}}{\mu_y F_z} \alpha \tag{4.16}$$

The friction coefficient may be assumed to depend on the slip velocity V_s. To model the situation on wet roads a decaying function $\mu(V_s)$ may be employed, cf. e.g. Eq.(4.E23).

When considering the computed characteristics of Fig.3.35c (2nd row) for small camber angles a horizontal shift of the F_y curve may give a reasonable result. Then, the peak side force remains unchanged which is a reasonable assumption but not always supported by experimental evidence (where often but not always a slight increase in maximum side force is manifested) or by computations with a physical model with constant friction and finite contact width which show a slight decrease. For small angles, the camber thrust is approximated by the product of the camber stiffness and the camber angle: $F_{y\gamma}=C_{F\gamma}\gamma$. Consequently, the α shift should amount to

$$S_{Hy} = \frac{C_{F\gamma}(F_z)}{C_{F\alpha}(F_z)} \gamma \tag{4.17}$$

so that

$$\alpha^* = \alpha + S_{Hy} \tag{4.18}$$

which gives rise to α_{eq} (4.16) with α replaced by $\alpha^* = \alpha + S_{Hy}$.

For the representation of the aligning moment at the new conditions the situation is more complex. We observe from Fig.3.35c that for not too large slip angles the original curve M_{zo} tends to both shift sideways and upwards. If the same equivalent slip angle and thus the same horizontal shift (4.17) as for the force is employed, the moment would become zero where also the force curve crosses the α axis. A moment equal to $-C_{M\alpha}S_{Hy}$ would arise at $\alpha = 0$. However, the moment should become equal to $C_{M\gamma}\gamma$, with a positive camber moment stiffness $C_{M\gamma}$. This implies that an additional vertical shift is required equal to:

$$S_{Vz} = C_{M\gamma}(F_z)\gamma + C_{M\alpha}(F_z)S_{Hy} \tag{4.19}$$

This additional moment corresponds to the so-called residual torque M_{zr}, which
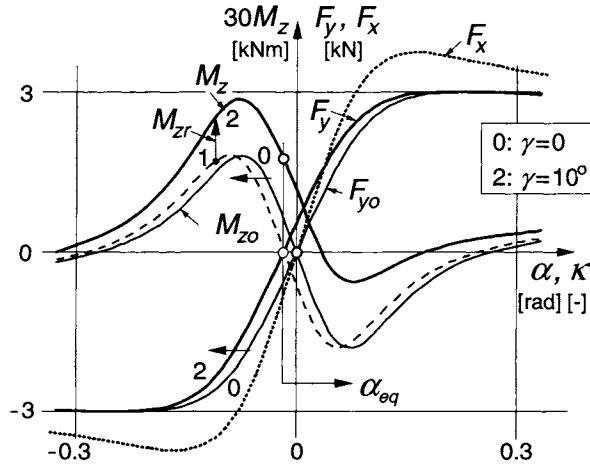
Fig. 4.5. Introduction of a camber angle in the side force and the aligning torque pure slip characteristics according to the similarity method. The longitudinal force pure slip characteristic. ($F_z = F_{zo} = 3000$N, $\mu_y = \mu_{yo} = 1$, $\mu_x = \mu_{xo} = 1.26$).

is the moment that remains when the side force becomes equal to zero. For larger values of the slip angle the additional moment should tend to zero as can be observed in Fig.3.35c. This may be easily accomplished by dividing (4.19) by a term like $1 + c_7\alpha^2$.

The dependencies of the camber stiffnesses on the vertical load may be assumed linear. We have:

$$C_{F\gamma} = c_5 F_z \, , \qquad C_{M\gamma} = c_6 \frac{b^2}{r_e} C_{F\kappa} \tag{4.20a}$$

where b denotes half the (assumedly constant) width of the contact patch, r_e the effective rolling radius and $C_{F\kappa}$ the longitudinal slip stiffness which is considered to be linearly increasing with load:

$$C_{F\kappa} = c_8 F_z \tag{4.20b}$$

In Fig.4.5 the different steps leading to the condition with a (small) camber angle have been demonstrated. First, the original curve (0) is moved to the left over a distance equal to the horizontal shift (4.17) yielding the intermediate curve (1). Then the residual torque is added: vertical shift (4.19), possibly made a function of slip angle by multiplying the shift with a decaying weighting function as suggested above. The load F_z and the friction coefficient μ_y have been kept equal to their reference values: 3000N and 1 respectively.

The longitudinal force at pure longitudinal slip may be modelled in the same

way as we did for the side force. Equations similar to (4.6-8) hold for the reference function. An influence of camber on the longitudinal force, however, is assumed not to occur. In the same Fig.4.5 the characteristic for F_x vs κ has been drawn. The values of the relevant additional parameters for the longitudinal force and the moment have been listed in Table 4.1.

We finally have the following similarity formulae for pure slip conditions (either at longitudinal or at lateral slip) for the longitudinal force:

$$F_x = \frac{\mu_x F_z}{\mu_{xo} F_{zo}} F_{xo}(\kappa_{eq}) \tag{4.21}$$

with the equivalent longitudinal slip

$$\kappa_{eq} = \frac{C_{F\kappa}(F_z)}{C_{F\kappa o}} \frac{\mu_{xo} F_{zo}}{\mu_x F_z} \kappa \tag{4.22}$$

and for the side force:

$$F_y = \frac{\mu_y F_z}{\mu_{yo} F_{zo}} F_{yo}(\alpha_{eq}) \tag{4.23}$$

with the equivalent slip angle, containing the horizontal shift (4.17):

$$\alpha_{eq} = \frac{C_{F\alpha}(F_z)}{C_{F\alpha o}} \frac{\mu_{yo} F_{zo}}{\mu_y F_z} \left(\alpha + \frac{C_{F\gamma}(F_z)}{C_{F\alpha}(F_z)} \gamma \right) \tag{4.24}$$

and for the aligning torque:

$$M_z = \frac{\mu_y F_z}{\mu_{yo} F_{zo}} \frac{C_{M\alpha}(F_z)}{C_{M\alpha o}} \frac{C_{F\alpha o}}{C_{F\alpha}(F_z)} M_{zo}(\alpha_{eq}) + M_{zr} \tag{4.25}$$

with the residual torque corresponding to the vertical shift (4.19) provided with the reduction factor:

$$M_{zr} = \frac{C_{M\gamma}(F_z) + t(F_z) C_{F\gamma}(F_z)}{1 + c_7 \alpha^2} \gamma \tag{4.26}$$

4.2.2. Combined Slip Conditions

We will now address the problem of describing the situation at combined slip. The analysis of the brush model has given considerable insight into the mechanisms that play a role and we will use the theoretical slip quantities $\sigma_{x,y}$ (3.34 or 3.32) and the magnitude σ (3.40) and we will adopt the concept similar to that of assessing the components of the resulting horizontal force according

to (3.49) and consider the pneumatic trail t as in (3.50) and include explicit contributions of F_x to the moment as indicated in (3.51). We have for the theoretical slip quantities with the α shift due to camber included:

$$\sigma_x = \frac{\kappa}{1 + \kappa} \tag{4.27a}$$

$$\sigma_y^* = \frac{\tan\alpha^*}{1 + \kappa} \tag{4.27b}$$

and

$$\sigma^* = \sqrt{\sigma_x^2 + \sigma_y^{*2}} \tag{4.28}$$

with

$$\alpha^* = \alpha + \frac{C_{F\gamma}(F_z)}{C_{F\alpha}(F_z)}\gamma \tag{4.29}$$

In the ensuing theory we will make use of the theoretical slip quantities (4.27a,b), which does produce the slope in the constant α curves in the F_y vs F_x diagram at $F_x = 0$. It should be noted, however, that experience has shown that the use of practical slip quantities s_x and s_y^* (that is: κ and $\tan\alpha^*$ which may be obtained again by omitting the denominators in (4.27a,b)) may already give very good results as will be indicated later on in Fig.4.8. Note that when approaching wheel lock $\sigma_x \rightarrow \infty$. This calls for an artificial limitation by adding a small positive quantity to the denominator of (4.27a).

Because we are dealing with an in general non-isotropic tyre we have pure longitudinal and lateral slip characteristics that are not identical (cf. Fig.4.5). Still, we will take the lateral and longitudinal components but then of the respective pure slip characteristics F_{yo} and F_{xo}. If we want to use the theoretical slip quantities σ we must have available the pure slip characteristics with σ_x and σ_y as abscissa. This can be accomplished by fitting the original data after having computed the values of σ_x for each value of κ by using (4.27a) and similar for transforming α into $\tan\alpha$ and denoting the resulting functions: $F_{xo}(\sigma_x)$, $F_{yo}(\sigma_y)$ and $M_{zo}(\sigma_y)$. Or, simpler, by replacing in the already available pure slip force and moment functions, expressed in terms of the practical slip quantities, the argument α (in radians) by $\tan\alpha$ (probably acceptable approximation) and κ by the expression given below (derived from Eq.(4.27a)).

$$\kappa = \frac{\sigma_x}{1 - \sigma_x} \tag{4.30}$$

which would be successful if the F_x characteristic had been fitted for the whole range of positive (driving) and negative (braking) values of κ. Otherwise if only
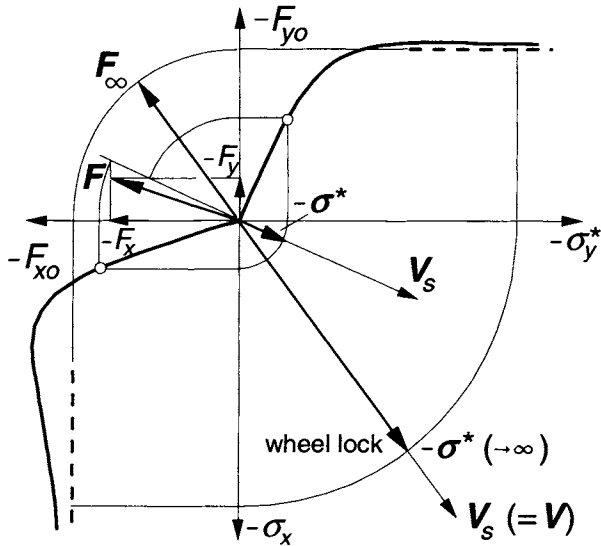
Fig. 4.6. Construction of the resulting combined slip force from the pure slip characteristics according to Eqs.(4.31).

the braking side is available (κ and σ_x <0) and the driving side is modelled as the mirror image of the braking side one might better take:

$$\kappa = \frac{\sigma_x}{1 + |\sigma_x|} \tag{4.30a}$$

If the thus obtained function of F_x is plotted vs σ_x the resulting curve becomes symmetric. However, if then the abscissa is transposed into κ by using (4.30) the resulting curve turns out to become asymmetric with the braking side identical to the characteristic we started out with. This asymmetry was already found to occur with the brush model discussed in Chapter 3.

Next, we should realise that through (4.18) camber has been accounted for and that, as a consequence, σ_y is to be replaced by σ_y^* defined by Eq.(4.27b). The resulting force and moment functions are denoted by $F_{xo}(\sigma_x)$, $F_{yo}(\sigma_y^*)$ and $M_{zo}(\sigma_y^*)$. As illustrated in Fig.4.6, the 'components' now become with σ^* denoting the magnitude of the theoretical slip vector (4.28):

$$F_x = \frac{\sigma_x}{\sigma^*} F_{xo}(\sigma^*) \ , \quad F_y = \frac{\sigma_y^*}{\sigma^*} F_{yo}(\sigma^*) \tag{4.31}$$

The figure shows how the force vector arises from the individual pure slip characteristics. At small slip, in general, the vector does not run opposite with respect to the slip speed vector V_s. At wheel lock, however, the force vector does

run opposite with respect to the slip speed vector because it is assumed here that the levels of the individual characteristics (asymptotes) are the same for the slip approaching infinity (in the Magic Formula we should have: $\mu_{yo}\sin(\tfrac{1}{2}\pi C_y) = \mu_{xo}\sin(\tfrac{1}{2}\pi C_x)$). At large slip the theory apparently fails to properly account for the contribution of the camber angle. At wheel lock one would expect the side force to become zero at vanishing slip angle. This will not exactly be the case in the model due to the equivalent theoretical side slip defined according to Eq.(4.27b) with α^* given by (4.18).

For the aligning torque we may define:

$$M_z = M_z' + M_{zr} - \frac{c_9 a_o}{F_{zo}} F_x F_y - c_{10} a_o F_x - c_{11} b \gamma F_x \qquad (4.32)$$

with the first term directly attributable to the side force. This term can be written as:

$$M_z' = -t(\sigma^*) \cdot F_y \qquad (4.33)$$

By considering (4.31) it turns out that (4.33) becomes:

$$M_z' = \frac{\sigma_y^*}{\sigma^*} M_{zo}'(\sigma^*) \qquad (4.34)$$

The last three terms of Eq.(4.32) result from the moment exerted by the longitudinal force because of the moment arm that arises through the side force induced deflection, a possibly initial offset of the line of action and the sideways rolling of the tyre cross section due to camber. For the sake of simplicity these effects are assumed not to be influenced by the wheel load.

With the similarity expressions for the pure slip forces $F_{x,yo}$ and moment M_{zo}' we finally obtain the following formulae for combined slip conditions. For the longitudal force:

$$F_x = \frac{\sigma_x}{\sigma^*} \frac{\mu_x F_z}{\mu_{xo} F_{zo}} F_{xo}(\sigma_{eq}^x) \qquad (4.35)$$

with the equivalent slip

$$\sigma_{eq}^x = \frac{C_{F\kappa}(F_z)}{C_{F\kappa o}} \frac{\mu_{xo} F_{zo}}{\mu_x F_z} \sigma^* \qquad (4.36)$$

and for the side force:

$$F_y = \frac{\sigma_y^*}{\sigma^*} \frac{\mu_y F_z}{\mu_{yo} F_{zo}} F_{yo}(\sigma_{eq}^y) \qquad (4.37)$$
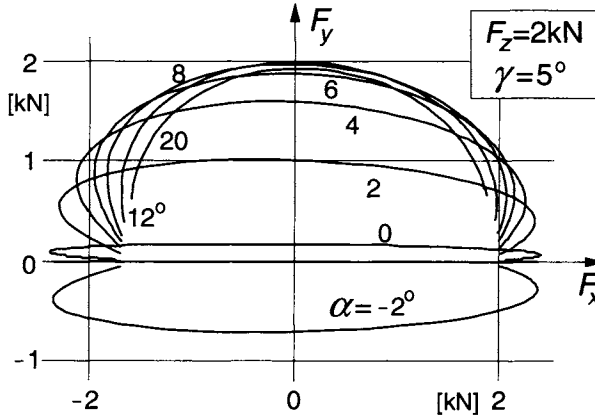
Fig. 4.7a. Cornering force vs longitudinal force at a new load and camber angle as computed
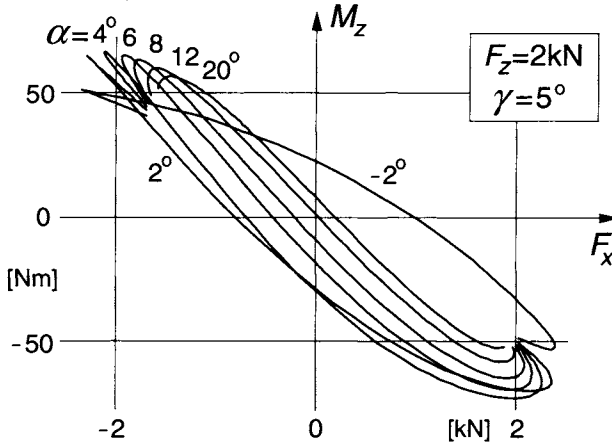   with the similarity method.

Fig. 4.7b. Aligning torque vs longitudinal force at a new load and camber angle as computed
      with the similarity method.

with the equivalent slip

$$\sigma_{eq}^{y} = \frac{C_{Fa}(F_z)}{C_{Fao}} \frac{\mu_{yo} F_{zo}}{\mu_y F_z} \sigma^* \tag{4.38}$$

and for the aligning torque:

$$M_z = \frac{\sigma_y^*}{\sigma^*} \frac{\mu_y F_z}{\mu_{yo} F_{zo}} \frac{C_{Ma}(F_z)}{C_{Mao}} \frac{C_{Fao}}{C_{Fa}(F_z)} M'_{zo}(\sigma_{eq}^y) + M_{zr} +$$
$$- \frac{c_9 a_o}{F_{zo}} F_x F_y - c_{10} a_o F_x - c_{11} b \gamma F_x \tag{4.39}$$

with the residual torque

$$M_{zr} = \frac{C_{M\gamma}(F_z) + t(F_z)\, C_{F\gamma}(F_z)}{1 + c_7(\sigma_{eq}^y)^2}\, \gamma \qquad (4.40)$$

On behalf of example calculations, the three additional non-dimensional parameters c_9, c_{10} and c_{11} have been given values listed in Table 4.1.

For the case of a load different from the reference value and the presence of a camber angle, the combined slip characteristics for the tyre side force and for the aligning torque have been assessed by using the above equations. The resulting diagrams with slip angle α used as parameter have been presented in the Figs.4.7a and b. Due to the use of the theoretical slip quantities (4.27a, 4.27b) we find that the curves of F_y show the slight slope near $F_x = 0$ also observed to occur with the physical brush model and sometimes more pronounced in experimentally assessed characteristics (Fig.3.18). The additional slope that arises when a camber angle is introduced (cf. Fig.3.35c, top) for which the torsional compliance is responsible does not appear. A special formulation would be needed to represent this effect. In the next section we will take care of this in connection with the *Magic Formula* tyre model.

It may be further remarked that the similarity model given by the equations (4.35-40) together with (4.27a,b), (4.28) and the reference pure slip functions does represent the actual tyre steady-state behaviour well in the following
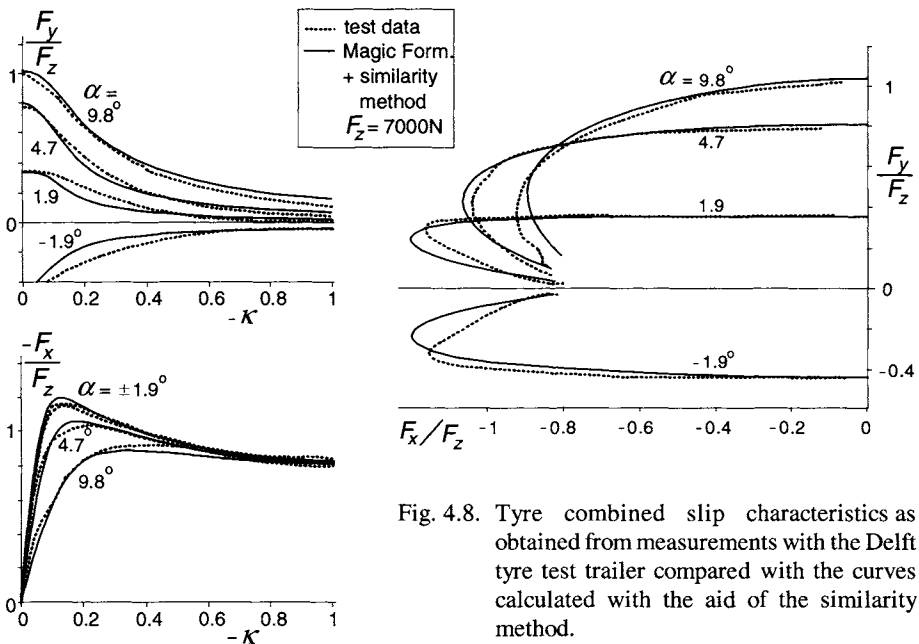

Fig. 4.8. Tyre combined slip characteristics as obtained from measurements with the Delft tyre test trailer compared with the curves calculated with the aid of the similarity method.

extreme cases: (1) in pure slip situations, (2) in the linearised combined slip situation (small α and κ) and (3) in the case of a locked wheel ($\gamma = 0$). As illustrated in Fig.4.6 the model correctly shows that when the wheel is locked, the resulting force acts in a direction opposite to the slip speed vector V_s if in the original reference pure slip curves the level of F_{xo} and of F_{yo} tend to the same level when both slip components approach infinity (governed by the parameters μ and C in the *Magic Formula*). Other combinations of slip may give rise to deviations with respect to measured characteristics. It is noted that when the terms for the aligning torque with parameters c_9, c_{10} and c_{11} are disregarded, the combined slip performance can be represented without the necessity to rely on combined slip measurement data.

A comparison with measured data is given in Fig.4.8. Here the similarity method is used where instead of the theoretical slip quantities the practical slip variables κ and $\tan\alpha$ have been employed. A relatively good agreement is achieved for this passenger car tyre in the combined slip situation.

4.2.3. Combined Slip Conditions with F_x as Input Variable

In more simple vehicle dynamics simulation studies with the wheel spin degree of freedom not included, one may prefer to use the longitudinal force F_x as input quantity instead of the longitudinal slip κ. This approach has been used, almost exclusively, in early vehicle dynamics research. However, for (quasi) steady-state cornering analysis, notably circuit simulation in the racing world, this option is still popular. An important limitation of using this method is the condition that the F_x vs κ characteristic (although not used) is supposed to show a positive slope over the entire range of longitudinal slip while at wheel lock $F_x = -\mu F_z$. Or, alternatively, we use only that part of the characteristic that lies in between the two peaks. This entails that the F_y vs F_x curves are single valued in the F_x range employed. Furthermore, it is assumed that the friction coefficient is the same for longitudinal and lateral directions and is denoted with μ.

The obvious main effect of the introduction of F_x on the side force is the lowering of the maximum side force that can be generated. For this to realise the right-hand expressions of Eqs.(4.23) and (4.25) are to be multiplied with the factor

$$\varphi_x = \frac{\sqrt{\mu^2 F_z^2 - F_x^2}}{\mu F_z} \tag{4.41}$$

while the expression (4.24) is to be divided by the same factor. The cornering

and aligning stiffnesses remain unaffected through this operation. These stiffnesses, however, do depend on the longitudinal force as becomes obvious from the curves of Fig.3.13 that belong to small side slip angles. The following functions may serve as a crude approximation of the actual relationships.

$$C_{F\alpha}(\mu,F_z,F_x) = \varphi_{x\alpha}\left\{C_{F\alpha}(F_z) - \tfrac{1}{2}\mu F_z\right\} + \tfrac{1}{2}(\mu F_z - F_x) \tag{4.42}$$

with

$$\varphi_{x\alpha} = \left\{1 - \left(\frac{F_x}{\mu F_z}\right)^n\right\}^{1/n} \tag{4.42a}$$

Depending on the user's desire one may choose for n a value in the range of 2 to 8 (more or less curved characteristic $C_{F\alpha}(F_x)$) . For the aligning stiffness we may use the formula:

$$C_{M\alpha}(\mu,F_z,F_x) = \varphi_x^2 C_{M\alpha}(F_z) \tag{4.43}$$

and similar for the camber stiffness:

$$C_{F\gamma}(\mu,F_z,F_x) = \varphi_x^2 C_{F\gamma}(F_z) \tag{4.44}$$

The camber moment stiffness may be disregarded. The load dependencies $C_{F,M\alpha}(F_z)$ and $C_{F\gamma}(F_z)$ of the freely rolling tyre already appeared in Eqs.(4.24, 4.25). It may be ascertained that the present model makes sure that the cornering stiffness vanishes when $F_x \to \mu F_z$ (wheel drive spin, $\kappa \to \infty$) while at $F_x = -\mu F_z$ (wheel lock, $\kappa = -1$) the side slip stiffness equals μF_z, which is correct. The functional relationships (4.21, 4.22) for F_x do not play a role anymore and the friction coefficient μ_y has been replaced by μ. The imposed longitudinal force should be kept within the boundaries $-\mu F_z \cos\alpha \leq F_x \leq \mu F_z$.

The resulting equations for the side force and the aligning torque with the longitudinal force serving as one of the input quantities now read:
For the side force:

$$F_y = \varphi_x \frac{\mu F_z}{\mu_o F_{zo}} F_{yo}(\alpha_{eq}) \tag{4.45}$$

with the equivalent slip angle

$$\alpha_{eq} = \frac{1}{\varphi_x} \frac{C_{F\alpha}(\mu,F_z,F_x)}{C_{F\alpha o}} \frac{\mu_o F_{zo}}{\mu F_z} \left(\alpha + \frac{C_{F\gamma}(\mu,F_z,F_x)}{C_{F\alpha}(\mu,F_z,F_x)}\gamma\right) \tag{4.46}$$

and for the aligning torque:

$$M_z = \varphi_x \frac{\mu F_z}{\mu_o F_{zo}} \frac{C_{M\alpha}(\mu,F_z,F_x)}{C_{M\alpha o}} \frac{C_{F\alpha o}}{C_{F\alpha}(\mu,F_z,F_x)} M_{zo}(\alpha_{eq}) + M_{zr} +$$

$$- \frac{c_9 a_o}{F_{zo}} F_x F_y - c_{10} a_o F_x - c_{11} b \gamma F_x \qquad (4.47)$$

where the last terms have been taken from (4.39) and the residual torque reads:

$$M_{zr} = \varphi_x \frac{C_{M\gamma}(F_z) + t(F_z) C_{F\gamma}(F_z)}{1 + c_7 \alpha^2} \gamma \qquad (4.48)$$

Exercise 4.1 given at the end of Section 4.3 addresses the problem of assessing the side force characteristics using the similarity technique with the longitudinal force considered as one of the input quantities.

In Section 4.3 the *Magic Formula* tyre model will be treated in detail. This complex model is considerably more accurate and will again employ the longitudinal slip κ as input variable.

4.3. The *Magic Formula* Tyre Model

A widely used semi-empirical tyre model to calculate steady-state tyre force and moment characteristics for use in vehicle dynamics studies is based on the so-called *Magic Formula*. The development of the model was started in the mid-eighties. In a cooperative effort TU-Delft and Volvo developed several versions (Bakker et al. 1987, 1989, Pacejka et al. 1993). In these models the combined slip situation was modelled from a physical view point. In 1993 Michelin (cf. Bayle et al. 1993) introduced a purely empirical method using *Magic Formula* based functions to describe the tyre horizontal force generation at combined slip. This approach was adopted by DVR (the Delft Vehicle Dynamics Research Center, a joint venture of TU-Delft and TNO-Delft). In the newer version of 'Delft-Tyre' the original description of the aligning torque is altered to accommodate a relatively simple physically based combined slip extension. The pneumatic trail is introduced as a basis to calculate this moment about the vertical axis, cf. Pacejka (1996). A complete listing of the model is given in Section 4.3.2. In Section 4.3.3 the model is further extended by introducing formulae for the description of the situation at large camber and turn slip.

4.3.1. Model Description

The general form of the formula that holds for given values of vertical load and camber angle reads:

$$y = D \sin[C \arctan\{Bx - E(Bx - \arctan Bx)\}]$$ (4.49)

with

$$Y(X) = y(x) + S_V$$ (4.50)

$$x = X + S_H$$ (4.51)

where

Y: output variable F_x, F_y or possibly M_z

X: input variable $\tan\alpha$ or κ

and

B stiffness factor

C shape factor

D peak value

E curvature factor

S_H horizontal shift

S_V vertical shift

The *Magic Formula* $y(x)$ typically produces a curve that passes through the origin $x = y = 0$, reaches a maximum and subsequently tends to a horizontal asymptote. For given values of the coefficients B, C, D and E the curve shows an anti-symmetric shape with respect to the origin. To allow the curve to have an offset with respect to the origin, two shifts S_H and S_V have been introduced. A new set of coordinates $Y(X)$ arises as shown in Fig.4.9. The formula is capable
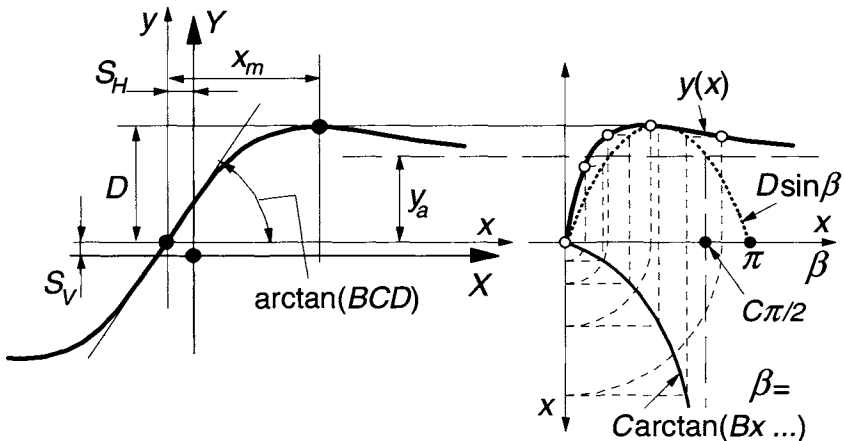

Fig. 4.9. Curve produced by the original sine version of the Magic Formula, Eq.(4.49). The meaning of curve parameters have been indicated.

of producing characteristics that closely match measured curves for the side
force F_y (and if desired also for the aligning torque M_z) and for the fore and aft
force F_x as functions of their respective slip quantities: the slip angle α and the
longitudinal slip κ with the effect of load F_z and camber angle γ included in the
parameters.

Figure 4.9 illustrates the meaning of some of the factors by means of a typical
side force characteristic. Obviously, coefficient D represents the peak value (with
respect to the central x-axis and for $C \geq 1$) and the product BCD corresponds to
the slope at the origin ($x = y = 0$). The shape factor C controls the limits of the
range of the sine function appearing in formula (4.49) and thereby determines the
shape of the resulting curve. The factor B is left to determine the slope at the
origin and is called the stiffness factor. The factor E is introduced to control the
curvature at the peak and at the same time the horizontal position of the peak.

From the heights of the peak and of the horizontal asymptote the shape factor
C may be computed:

$$C = 1 \pm \left(1 - \frac{2}{\pi} \arcsin \frac{y_a}{D} \right) \qquad (4.52)$$

From B and C and the location x_m of the peak the value of E may be assessed:

$$E = \frac{B x_m - \tan\{\pi/(2C)\}}{B x_m - \arctan(B x_m)} \quad (\text{if } C > 1) \qquad (4.53)$$

The offsets S_H and S_V appear to occur when ply-steer and conicity effects and
possibly the rolling resistance cause the F_y and F_x curves not to pass through the
origin. Wheel camber may give rise to a considerable offset of the F_y vs α curves.
Such a shift may be accompanied by a significant deviation from the pure anti-
symmetric shape of the original curve (cf. Fig.3.35c,d). To accommodate such
an asymmetry, the curvature factor E is made dependent of the sign of the
abscissa (x).

$$E = E_o + \Delta E \cdot \mathrm{sgn}(x) \qquad (4.54)$$

Also the difference in shape that is expected to occur in the F_x vs κ characteristic
between the driving and braking ranges can be taken care of. In Fig.4.10 the
influence of the two shape factors C and E on the appearance of the curves have
been demonstrated. The diagrams have been normalised by dividing y by D and
multiplying x with CB making the curve peak level and initial slope independent
of the parameters.

In rather extreme cases, the sharpness that can be reached by means of the
function given by Eq.(4.49) may not be sufficient. It turns out to be possible to
considerably increase the sharpness of the curves by introducing an extra term
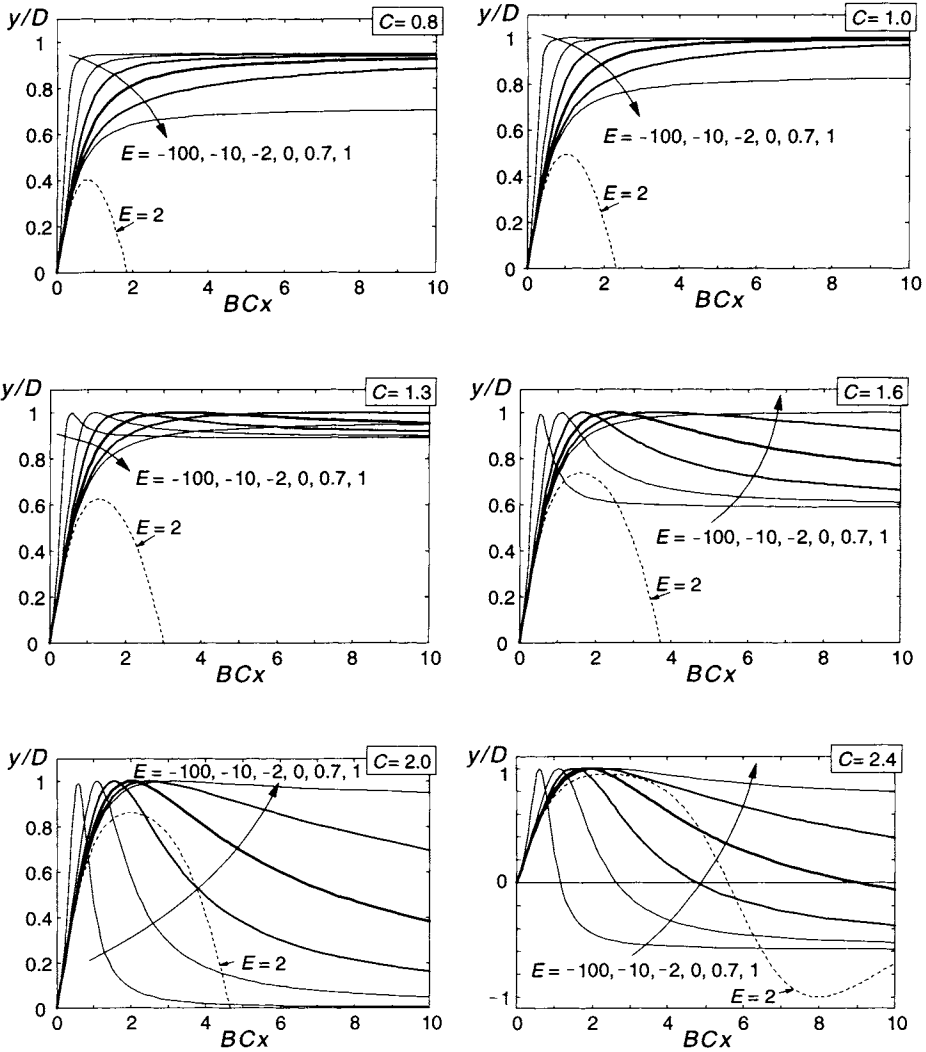
Fig. 4.10. The influence of the shape factors C and E on the appearance of the curve according to Eq.(4.49). Note that a value of curvature factor $E > 1$ does not produce realistic curves.

in the argument of the arctan function. The modified function reads:

$$y = D \sin[C \arctan\{Bx - E(Bx - \arctan Bx) + H \arctan^7 Bx\}] \qquad (4.55)$$

Figure 4.11 demonstrates the effect of the new coefficient H. Too large values may give rise to an upward curvature of the curve near the origin as would also
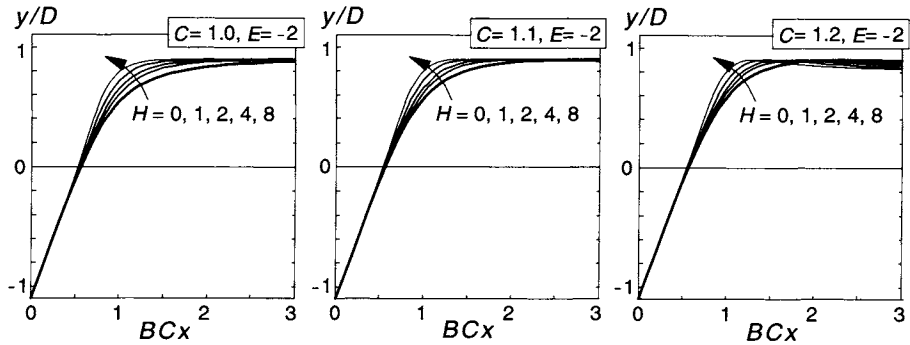
Fig. 4.11. Sharpness of curves near the peak may be increased by introducing additional term
with sharpness factor H (according to Eq.(4.55)).

occur at large negative values of E (cf. the lower diagrams of Fig.4.10). In the
ensuing text we will not use this additional coefficient H.

It may be furthermore of interest to note that the possibly awkward function
$\arctan(x)$ may be replaced by the possibly faster and almost identical pseudo
arctan function $psatan(x) = x(1+a|x|)/\{1+2(b|x|+ax^2)/\pi\}$ with $a = 1.1$ and $b = 1.6$.

The various factors are functions of normal load and wheel camber angle.
Several parameters appear in these functions. A suitable regression technique is
used to determine their values from measured data according to a quadratic
algorithm for the best fit (cf. Oosten and Bakker 1993). One of the important
functional relationships is the variation of the cornering stiffness (almost exactly
given by the product of the coefficients B_y, C_y and D_y of the side force function:
$BCD_y = K_{y\alpha} = \partial F_y/\partial\alpha$ at $\tan\alpha = -S_H$) with F_z and γ.

$$BCD_y = p_1 \sin[2\arctan(F_z/p_2)]/(1+p_3\gamma^2) \qquad (4.56)$$

For zero camber, the cornering stiffness attains its maximum p_1 at $F_z = p_2$. In
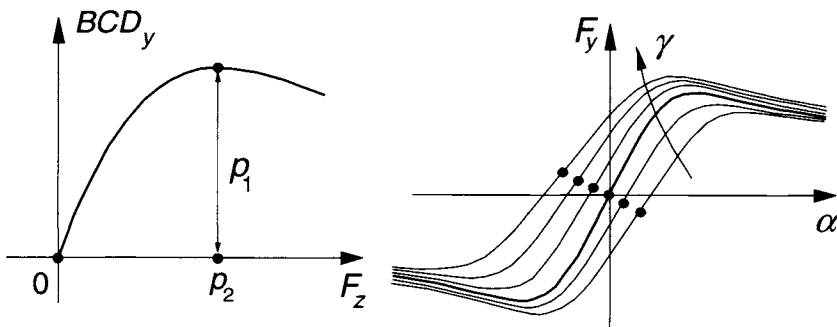

Fig. 4.12. Cornering stiffness vs vertical load and the influence of wheel camber, Eq. (4.56).
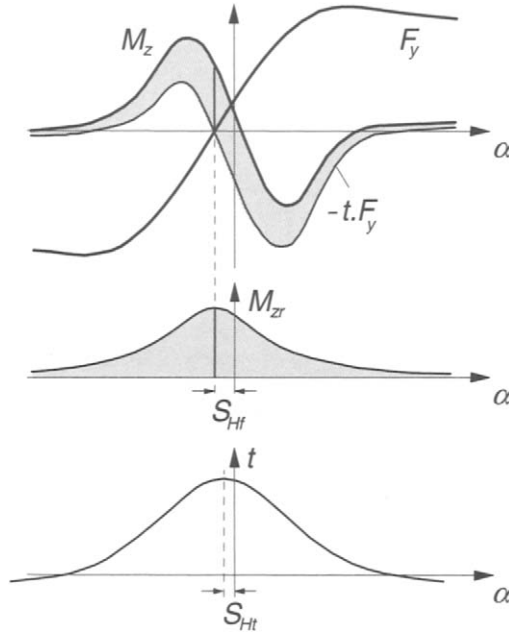
Fig. 4.13. The aligning torque characteristic composed of a part directly attributed to the side force and a part due the so-called residual torque (due to tyre conicity and camber).

Fig.4.12 the basic relationship has been depicted. Apparently, for a cambered wheel the cornering stiffness decreases with increasing $|\gamma|$. Note the difference in curvature left and right of the characteristics at larger values of the camber angle. To accomplish this, a split-E according to Eq.(4.54) has been employed. We refer to Section 4.3.2 for a complete listing of the formulae. Here, non-dimensional parameters have been introduced. For example, the parameters in (4.56) will become: $p_1 = F_{zo} p_{Ky1}$, $p_2 = F_{zo} p_{Ky2}$ and $p_3 = p_{Ky3}$, with F_{zo} denoting the nominal wheel load.

The aligning torque M_z can now be obtained by multiplying the side force F_y with the pneumatic trail t and adding the usually small (except with camber) residual torque M_{zr} (cf. Fig.4.13). We have:

$$M_z = -t \cdot F_y + M_{zr} \tag{4.57}$$

The pneumatic trail decays with increasing side slip and is described as follows:

$$t(\alpha_t) = D_t \cos[C_t \arctan\{B_t \alpha_t - E_t (B_t \alpha_t - \arctan(B_t \alpha_t))\}] \tag{4.58}$$

where

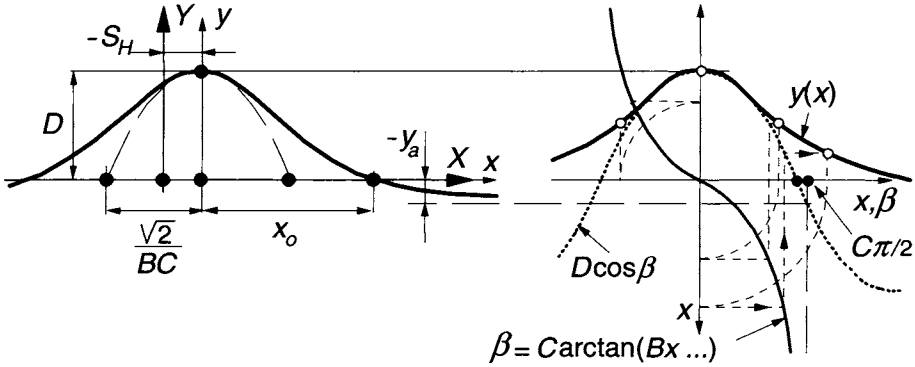$$\alpha_t = \tan\alpha + S_{Ht} \tag{4.59}$$

Fig. 4.14. Curve produced by the cosine version of the *Magic Formula*, Eq.(4.58). The meaning of curve parameters have been indicated.

The residual torque showing a similar decay:

$$M_{zr}(\alpha_r) = D_r \cos[\arctan(B_r\alpha_r)] \tag{4.60}$$

with

$$\alpha_r = \tan\alpha + S_{Hf} \tag{4.61}$$

It is seen that both parts of the moment are modelled using the *Magic Formula*, but instead of the sine function, the cosine function is employed. In that way a hill-shaped curve is produced. The peaks are shifted sideways.

The residual torque is assumed to attain its maximum D_r at the slip angle where the side force becomes equal to zero. This is accomplished through the horizontal shift S_{Hf}. The peak of the pneumatic trail occurs at $\tan\alpha = -S_{Ht}$. This formulation has proven to give very good agreement with measured curves. The advantage with respect to the earlier versions, where formula (4.49) is used for the aligning torque as well, is that we have now directly assessed the function for the pneumatic trail which is needed to handle the combined slip situation.

In Fig.4.14 the basic properties of the cosine based curve have been indicated (subscripts of factors have been deleted again). Again, D is the peak value, C is a shape factor determining the level y_a of the horizontal asymptote and now B influences the curvature at the peak (illustrated with the inserted parabola). Factor E modifies the shape at larger values of slip and governs the location x_o of the point where the curve intersects the x axis. The following formulae hold:

$$C = \frac{2}{\pi}\arccos\frac{y_a}{D} \tag{4.62}$$

$$E = \frac{Bx_o - \tan\{\pi/(2C)\}}{Bx_o - \arctan(Bx_o)} \quad (\text{if } C>1) \tag{4.63}$$

In case of the possible presence of large camber angles (motorcycles) it may be better to use in (4.57) the side force F_y that would arise at $\gamma = 0$. Also, the side force function (4.49) and the cornering stiffness function (4.56) may be modified to better approximate large camber response for motorcycle tyres, cf. De Vries (1998a) and Sec. 11.6 for a full listing of equations. We refer to Section 4.3.3 for the discussion of the model extension for larger camber and turn slip (path curvature) also applicable in case of combined slip with braking or driving forces.

In the paper of Pacejka and Bakker (1993) the tyre's response to combined slip was modelled by using physically based formulae. A newer more efficient way is purely empiric. This method was developed by Michelin and published by Bayle, Forissier and Lafon (1993). It describes the effect of combined slip on the lateral force and on the longitudinal force characteristics. Weighting functions G have been introduced which when multiplied with the original pure slip functions (4.49) produce the interaction effects of κ on F_y and of α on F_x. The weighting functions have a hill shape. They take the value one in the special case of pure slip (κ or α equal to zero). When, for example, at a given slip angle a from zero increasing brake slip is introduced, the relevant weighting function for F_y may first show a slight increase in magnitude (becoming larger than one) but will soon reach its peak after which a continuous decrease follows. The cosine version of the Magic Formula is used to represent the hill shaped function:

$$G = D \cos[C \arctan(Bx)] \tag{4.64}$$

Here, G is the resulting weighting factor and x is either κ or $\tan\alpha$ (possibly shifted). The coefficient D represents the peak value (slightly deviating from one if a horizontal shift of the hill occurs), C determines the height of the hill's base and B influences the sharpness of the hill. Coefficient B constitutes the main factor responsible for the shape of the weighting functions.

As an extension to the original function published by Bayle et al., the part with shape factor E will be added later on. This extension appears to improve the approximation, in particular at large levels of slip, especially in view of the strict condition that the weighting function G must remain positive for all slip conditions.

For the side force we get the following formulae:

$$F_y = G_{y\kappa} \cdot F_{yo} + S_{Vy\kappa} \tag{4.65}$$

with the weighting function now expressed such that it equals unity at $\kappa = 0$:

$$G_{y\kappa} = \frac{\cos[C_{y\kappa}\arctan(B_{y\kappa}\kappa_S)]}{\cos[C_{y\kappa}\arctan(B_{y\kappa}S_{Hy\kappa})]} \quad (>0) \tag{4.66}$$

where

$$\kappa_S = \kappa + S_{Hy\kappa} \tag{4.67}$$

and further the coefficients

$$B_{y\kappa} = r_{By1} \cos[\arctan\{r_{By2}(\tan\alpha - r_{By3})\}] \tag{4.68a}$$

$$C_{y\kappa} = r_{Cy1} \tag{4.68b}$$

$$S_{Hy\kappa} = r_{Hy1} + r_{Hy2}df_z \tag{4.68c}$$

$$S_{Vy\kappa} = D_{Vy\kappa} \sin[r_{Vy5} \arctan(r_{Vy6}\kappa)] \tag{4.69a}$$

$$D_{Vy\kappa} = \mu_y F_z \cdot (r_{Vy1} + r_{Vy2}df_z + r_{Vy3}\gamma) \cdot \cos[\arctan(r_{Vy4}\tan\alpha)] \tag{4.69b}$$

with df_z the notation for the non-dimensional increment of the vertical load with respect to the (adapted) nominal load, cf. next Subsection 4.3.2, Eq.(4.E2). Figure 4.15 depicts the two weighting functions displayed both as functions of α and of κ and the resulting force characteristics (parameters according to Table 4.2 at end of Sec.4.3.3). Below, an explanation is given.

In Eq.(4.65) F_{yo} denotes the side force at pure side slip obtained from Eq.(4.49). The denominator of the weighting function (4.66) makes $G_{y\kappa}=1$ at $\kappa = 0$. The horizontal shift $S_{Hy\kappa}$ of the weighting function accomplishes the slight increase that the side force experiences at moderate braking before the peak of $G_{y\kappa}$ is reached and the decay of F_y commences. This horizontal shift may be made dependent on the vertical load. $C_{y\kappa}$ controls the level of the horizontal asymptote. If $C_{y\kappa}=1$ the weighting function (4.66) will approach zero when $\kappa \to \pm\infty$. This would be the correct value for $C_{y\kappa}$ if κ is expected to be used in the entire range from plus to minus infinity. If this is not intended then $C_{y\kappa}$ may be chosen different from one if $G_{y\kappa}$ is optimised with the restriction to remain positive. The factor $B_{y\kappa}$ influences the sharpness of the hill shaped weighting function. As indicated, the hill becomes more flat (wider) at larger slip angles. Then $B_{y\kappa}$ decreases according to (4.68a). When in an extreme situation α approaches $90°$, that is when $V_{cx} \to 0$, $B_{y\kappa}$ will go to zero and, consequently, $G_{y\kappa}$ will remain equal to one unless κ goes to infinity which may easily be the case when at $V_{cx} \to 0$ the wheel speed of revolution Ω and thus the longitudinal slip velocity V_{sx} remains unequal to zero. The quantity $S_{Vy\kappa}$ is the vertical 'shift', which sometimes is referred to as the κ-induced ply-steer. At camber, due to the added asymmetry, the longitudinal force clearly produces a torque that creates a torsion angle comparable with a possibly already present ply-steer angle. This shift function varies with slip κ indicated in (4.69a).
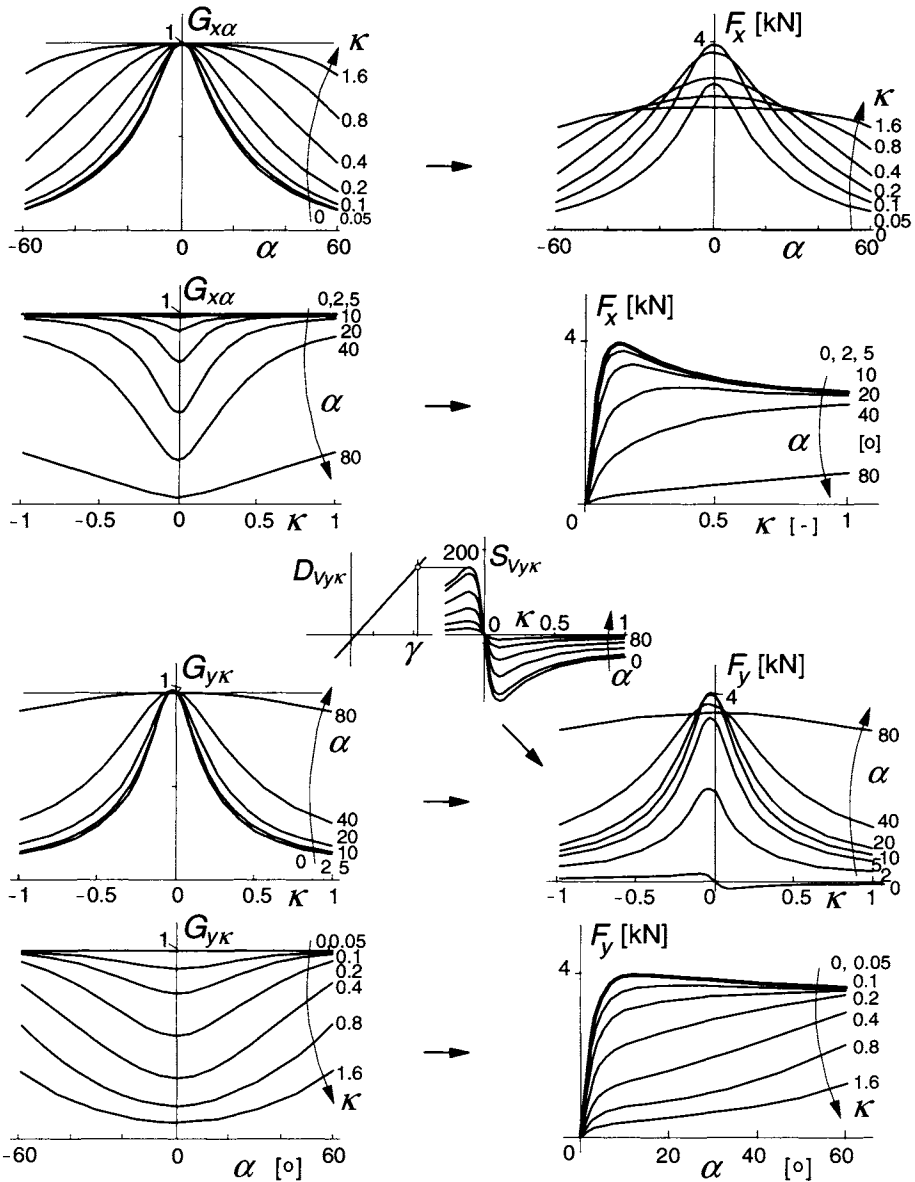
Fig. 4.15. Nature of weighting functions and the resulting combined slip longitudinal and lateral forces, the latter also affected by the κ induced ply-steer 'vertical shift' $S_{Vy\kappa}$.

As illustrated in Fig.4.15, its peak value $D_{Vy\kappa}$ depends on the camber angle γ and decays with increasing magnitude of the slip angle α. Figure 4.16 presents measured data together with the fitted curves as published by Bayle et al..

The combined slip relations for F_x are similar to what we have seen for the side force. However, a vertical shift function was not needed. In Fig.4.17 a three-dimensional graph is shown indicating the variation of F_x and F_y with both α and κ. The initial 'S' shape of the F_y vs κ curves (at small α) due to the vertical shift function is clearly visible.

For possible improvement of the general tendency of the model at larger levels of combined slip beyond the range of available test data one might include additional 'fabricated' data which are derived from similarity method results at larger values of the slip angle. Another possibility is the usage of the conditions at wheel lock where one might assume that the force and slip vector are co-linear. We then have for the ratio of the components:

$$\frac{F_x}{F_y} = \frac{V_{sx}}{V_{sy}} = \frac{\kappa}{\tan\alpha} = \frac{-1}{\tan\alpha} \qquad (4.70)$$

or

$$F_x = F_{xo(\kappa=-1)} \cdot \cos\alpha = F_{xo(\kappa=-1)} \cdot \frac{V_{sx}}{V_s} \qquad (4.71)$$

$$F_y = -F_{xo(\kappa=-1)} \cdot \sin\alpha = F_{xo(\kappa=-1)} \cdot \frac{V_{sy}}{V_s} \qquad (4.72)$$
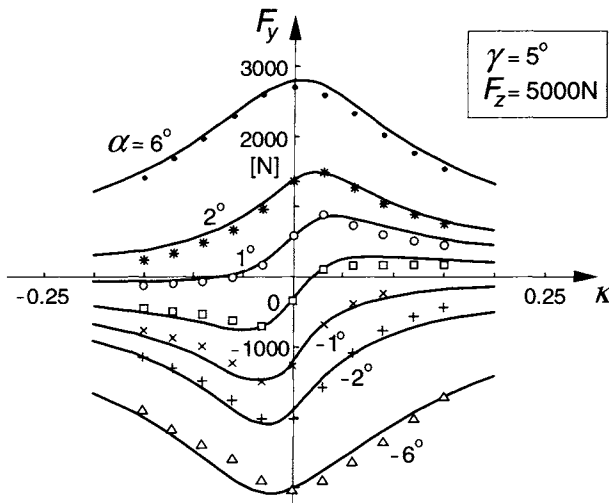

Fig. 4.16. The combined slip side force characteristics in the presence of a camber angle, Bayle et al. (1993).
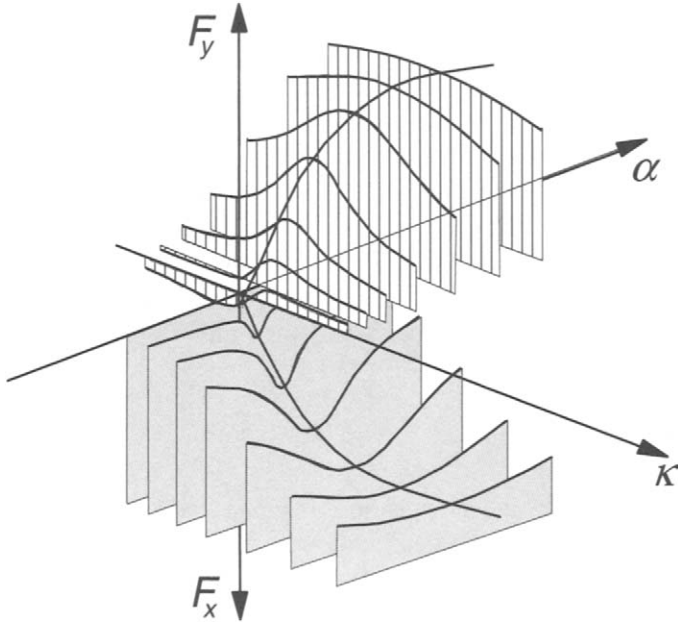
Fig. 4.17. Three-dimensional graph of combined slip force characteristics.

Regarding the aligning torque, physical insight is used to model the situation at combined slip. We write:

$$M_z = -t(\alpha_{t,eq}) \cdot F_y + M_{zr}(\alpha_{r,eq}) + s(F_y, \gamma) \cdot F_x \qquad (4.73)$$

The arguments α_t and α_r (including a shift) appearing in the functions (4.59, 4.61) for the pneumatic trail and residual torque at pure side slip are replaced by equivalent slip angles, as indicated by Eq.(4.74), incorporating the effect of κ on the composite slip.

$$\alpha_{t,eq} = \sqrt{\alpha_t^2 + \left(\frac{K_{x\kappa}}{K_{y\alpha}}\right)^2 \kappa^2} \cdot \text{sgn}(\alpha_t) \qquad (4.74)$$

and similar for $\alpha_{r,eq}$. To approximate the same effect on the degree of sliding in the contact patch as would occur with side slip, the longitudinal slip κ is multiplied with the ratio of the longitudinal and lateral slip stiffnesses.

Besides, an extra term is introduced in (4.73) to account for the fact that a moment arm s arises for F_x as a result of camber γ and lateral tyre deflection related to F_y. This extra term may give rise to a sign change of the aligning

torque in the range of braking as discussed before (cf. Fig.3.20).

The complete set of steady-state formulae has been listed in the subsequent section. Parameters p, q, r and s of the model are non-dimensional quantities. In addition, user scaling factors λ have been introduced. With that tool the effect of changing friction coefficient, cornering stiffness, camber stiffness etc. can be quickly investigated in a qualitative way without having the need to implement a completely new tyre data set. Scaling is done in such a way that realistic relationships are maintained. For instance, when changing the cornering stiffness and the friction coefficient in lateral direction (through $\lambda_{K_{y\alpha}}$ and $\lambda_{\mu y}$), the abscissa of the pneumatic trail characteristic is changed in a way equal to that of the side force characteristic and in accordance with the similarity method of Section 4.2.

4.3.2. Full Set of Equations

The *Magic Formula* model equations contain the non-dimensional model parameters p, q, r and s and, in addition, a set of scaling factors λ. Other parameters and variable quantities used in the equations are:

g acceleration due to gravity,

V_c magnitude of the velocity of the wheel contact centre C,

$V_{cx,y}$ components of the velocity of the wheel contact centre C,

$V_{sx,y}$ components of slip velocity V_s (of point S) with $V_{sy} \approx V_{cy}$, cf. Eq.(2.13),

V_r $(=R_e \Omega = V_{cx} - V_{sx})$ forward speed of rolling,

V_o reference velocity $(=\sqrt{(gR_o)}$ or other specified value),

R_o unloaded tyre radius $(=r_o)$,

R_e effective rolling radius $(=r_e)$,

Ω wheel speed of revolution

ρ_z tyre radial deflection (>0 if compression),

F_{zo} nominal (rated) load (≥ 0),

F'_{zo} adapted nominal load

The effect of having a tyre with a different nominal load may be roughly approximated by using the scaling factor λ_{Fzo}

$$F'_{zo} = \lambda_{Fzo} F_{zo} \qquad\qquad (4.E1)$$

Further, we introduce the normalised change in vertical load

$$df_z = \frac{F_z - F'_{zo}}{F'_{zo}} \qquad\qquad (4.E2)$$

Instead of taking the slip angle α itself (in radians, from Eq.(2.12)) as input quantity one may in case of very large slip angles and possibly backwards

running of the wheel better use the tangent of the slip angle defined as the lateral slip:

$$\alpha^* = \tan\alpha \cdot \mathrm{sgn}V_{cx} = -\frac{V_{cy}}{|V_{cx}|} \qquad (4.\mathrm{E}3)$$

For the spin due to the camber angle we introduce

$$\gamma^* = \sin\gamma \qquad (4.\mathrm{E}4)$$

The longitudinal slip ratio is defined as follows:

$$\kappa = -\frac{V_{sx}}{|V_{cx}|} \qquad (4.\mathrm{E}5)$$

If the forward speed V_{cx} becomes or is equal to zero one might add a small quantity ε in the denominator of (4.E3, 4.E5) to avoid singularity, or, when transient slip situations occur, one should use the transient slip quantities (or deformation gradients) $\tan\alpha'$ and κ' as defined and used in Chapters 7 and 8.

To avoid the occurrence of similar singularities in the ensuing equations due to e.g. zero velocity or zero vertical load, a small additional quantity ε (with same sign as its neighbouring main quantity) will be introduced in relevant denominators like in the next equation.

For the factor $\cos\alpha$ appearing in the equations for the aligning torque to properly handle the case of large slip angles and possibly backwards running ($V_{cx} < 0$) we have defined:

$$\cos'\alpha = \frac{V_{cx}}{V'_c} \qquad (4.\mathrm{E}6)$$

with

$$V'_c = V_c + \varepsilon_V \qquad (4.\mathrm{E}6\mathrm{a})$$

where we may choose $\varepsilon_V = 0.1$.

For the normally encountered situations where turn slip may be neglected (path radius $R \to \infty$) and camber remains small, the factors ζ_i appearing in the equations, are to be set equal to unity:

$$\zeta_i = 1 \qquad (i = 0, 1, ..., 8)$$

In the following Section 4.3.3 where the influence of spin (turn slip and camber) is described in the extended *Magic Formula* model, the proper expressions will be given for these factors and additional equations will be introduced.

User Scaling Factors

The following set of scaling factors λ is available. The default value of these factors is set equal to one (except $\lambda_{\mu V}$ which equals zero if not used). We have:

pure slip

λ_{Fzo}	nominal (rated) load
$\lambda_{\mu x,y}$	peak friction coefficient
$\lambda_{\mu V}$	with slip speed V_s decaying friction
$\lambda_{Kx\kappa}$	brake slip stiffness
$\lambda_{Ky\alpha}$	cornering stiffness
$\lambda_{Cx,y}$	shape factor
$\lambda_{Ex,y}$	curvature factor
$\lambda_{Hx,y}$	horizontal shift
$\lambda_{Vx,y}$	vertical shift
$\lambda_{Ky\gamma}$	camber force stiffness
$\lambda_{Kz\gamma}$	camber torque stiffness
λ_t	pneumatic trail (effecting aligning torque stiffness)
λ_{Mr}	residual torque

combined slip

$\lambda_{x\alpha}$	α influence on $F_x(\kappa)$
$\lambda_{y\kappa}$	κ influence on $F_y(\alpha)$
$\lambda_{Vy\kappa}$	κ induced 'ply-steer' F_y
λ_s	M_z moment arm of F_x

other

λ_{Cz}	radial tyre stiffness
λ_{Mx}	overturning couple stiffness
λ_{My}	rolling resistance moment

To change from a relatively high friction surface to a low friction surface the factors $\lambda_{\mu x}$ and $\lambda_{\mu y}$ may be given a value lower than unity. In addition, to reflect a slippery surface (wet) with friction decaying with increasing (slip) speed one may chose for $\lambda_{\mu V}$ a value larger than zero, e.g. Eqs.(4.E13,4.E23). The publications of Dijks (1974) and of Reimpell et al. (1986) may be useful in this respect. Note, that the slip stiffnesses are not affected through these changes. For the composite friction scaling factor, in x and y direction respectively, we have:

$$\lambda_{\mu x,y}^* = \lambda_{\mu x,y}/(1 + \lambda_{\mu V} V_s/V_o) \qquad\qquad (4.\text{E}7)$$

A special degressive friction factor $\lambda_{\mu x,y}'$ is introduced to recognise the fact that vertical shifts of the force curves do vanish when $\mu \to 0$ but at a much slower rate.

$$\lambda_{\mu x,y}' = A_\mu \lambda_{\mu x,y}^*/\{1 + (A_\mu - 1)\lambda_{\mu x y}^*\} \quad (\text{suggestion: } A_\mu = 10) \qquad (4.\text{E}8)$$

For the three forces and three moments acting from road to tyre and defined according to the diagram of Fig.2.3, the equations, first those for the condition of pure slip (including camber) and subsequently those for the condition of combined slip, read (version 2004):

Longitudinal Force (pure longitudinal slip)

$$F_{xo} = D_x \sin[C_x \arctan\{B_x \kappa_x - E_x(B_x \kappa_x - \arctan(B_x \kappa_x))\}] + S_{Vx} \qquad (4.E9)$$

$$\kappa_x = \kappa + S_{Hx} \qquad (4.E10)$$

$$C_x = p_{Cx1} \cdot \lambda_{Cx} \qquad (>0) \qquad (4.E11)$$

$$D_x = \mu_x \cdot F_z \cdot \zeta_1 \qquad (>0) \qquad (4.E12)$$

$$\mu_x = (p_{Dx1} + p_{Dx2} df_z) \cdot \lambda_{\mu x}^* \qquad (>0) \qquad (4.E13)$$

$$E_x = (p_{Ex1} + p_{Ex2} df_z + p_{Ex3} df_z^2) \cdot \{1 - p_{Ex4} \text{sgn}(\kappa_x)\} \cdot \lambda_{Ex} \qquad (\leq 1) \qquad (4.E14)$$

$$K_{x\kappa} = F_z \cdot (p_{Kx1} + p_{Kx2} df_z) \cdot \exp(p_{Kx3} df_z) \cdot \lambda_{Kx\kappa}$$
$$(= B_x C_x D_x = \partial F_{xo}/\partial \kappa_x \quad \text{at } \kappa_x = 0) \quad (= C_{F\kappa}) \qquad (4.E15)$$

$$B_x = K_{x\kappa}/(C_x D_x + \varepsilon_x) \qquad (4.E16)$$

$$S_{Hx} = (p_{Hx1} + p_{Hx2} df_z) \cdot \lambda_{Hx} \qquad (4.E17)$$

$$S_{Vx} = F_z \cdot (p_{Vx1} + p_{Vx2} df_z) \cdot \{|V_{cx}|/(\varepsilon_{Vx} + |V_{cx}|)\} \cdot \lambda_{Vx} \cdot \lambda_{\mu x}' \cdot \zeta_1 \qquad (4.E18)$$

Lateral Force (pure side slip)

$$F_{yo} = D_y \sin[C_y \arctan\{B_y \alpha_y - E_y(B_y \alpha_y - \arctan(B_y \alpha_y))\}] + S_{Vy} \qquad (4.E19)$$

$$\alpha_y = \alpha^* + S_{Hy} \qquad (4.E20)$$

$$C_y = p_{Cy1} \cdot \lambda_{Cy} \qquad (>0) \qquad (4.E21)$$

$$D_y = \mu_y \cdot F_z \cdot \zeta_2 \qquad (4.E22)$$

$$\mu_y = \{(p_{Dy1} + p_{Dy2} df_z)/(1 + p_{Dy3}\gamma^{*2})\} \cdot \lambda_{\mu y}^* \qquad (>0) \qquad (4.E23)$$

$$E_y = (p_{Ey1} + p_{Ey2} df_z)\{1 + p_{Ey5}\gamma^{*2} - (p_{Ey3} + p_{Ey4}\gamma^*)\text{sgn}(\alpha_y)\} \cdot \lambda_{Ey} \qquad (\leq 1) \qquad (4.E24)$$

$$K_{y\alpha} = p_{Ky1} F_{zo}' \sin[p_{Ky4} \arctan\{F_z/((p_{Ky2} + p_{Ky5}\gamma^{*2})F_{zo}')\}]/(1 + p_{Ky3}\gamma^{*2}) \cdot \zeta_3 \cdot \lambda_{Ky\alpha}$$
$$(= B_y C_y D_y = \partial F_{yo}/\partial \alpha_y \text{ at } \alpha_y = 0) \text{ (if } \gamma = 0: = K_{y\alpha o} = C_{F\alpha}) \text{ (usually: } p_{Ky4} = 2)$$
$$(4.E25)$$

$$B_y = K_{y\alpha}/(C_y D_y + \varepsilon_y) \tag{4.E26}$$

$$S_{Hy} = (p_{Hy1} + p_{Hy2} df_z) \cdot \lambda_{Hy} + (K_{y\gamma o} \gamma^* - S_{Vy\gamma}) \cdot \zeta_0 / (K_{y\alpha} + \varepsilon_K) + \zeta_4 - 1 \tag{4.E27}$$

$$S_{Vy\gamma} = F_z \cdot (p_{Vy3} + p_{Vy4} df_z) \gamma^* \cdot \lambda_{Ky\gamma} \cdot \lambda'_{\mu y} \cdot \zeta_2 \tag{4.E28}$$

$$S_{Vy} = F_z \cdot (p_{Vy1} + p_{Vy2} df_z) \cdot \lambda_{Vy} \cdot \lambda'_{\mu y} \cdot \zeta_2 + S_{Vy\gamma} \tag{4.E29}$$

$$K_{y\gamma o} = F_z \cdot (p_{Ky6} + p_{Ky7} df_z) \lambda_{Ky\gamma} \quad (= \sim \partial F_{yo}/\partial\gamma \text{ at } \alpha = \gamma = 0) \quad (= C_{F\gamma}) \tag{4.E30}$$

Aligning Torque (pure side slip)

$$M_{zo} = M'_{zo} + M_{zro} \tag{4.E31}$$

$$M'_{zo} = -t_o \cdot F_{yo} \tag{4.E32}$$

$$t_o = t(\alpha_t) = D_t \cos[C_t \arctan\{B_t\alpha_t - E_t(B_t\alpha_t - \arctan(B_t\alpha_t))\}] \cdot \cos'\alpha \tag{4.E33}$$

$$\alpha_t = \alpha^* + S_{Ht} \tag{4.E34}$$

$$S_{Ht} = q_{Hz1} + q_{Hz2} df_z + (q_{Hz3} + q_{Hz4} df_z)\gamma^* \tag{4.E35}$$

$$M_{zro} = M_{zr}(\alpha_r) = D_r \cos[C_r \arctan(B_r\alpha_r)] \tag{4.E36}$$

$$\alpha_r = \alpha^* + S_{Hf} \quad (= \alpha_f) \tag{4.E37}$$

$$S_{Hf} = S_{Hy} + S_{Vy}/K'_{y\alpha} \tag{4.E38}$$

$$K'_{y\alpha} = K_{y\alpha} + \varepsilon_K \tag{4.E39}$$

$$B_t = (q_{Bz1} + q_{Bz2} df_z + q_{Bz3} df_z^2) \cdot (1 + q_{Bz5}|\gamma^*| + q_{Bz6}\gamma^{*2}) \cdot \lambda_{Ky\alpha}/\lambda^*_{\mu y} \quad (>0) \tag{4.E40}$$

$$C_t = q_{Cz1} \qquad (>0) \tag{4.E41}$$

$$D_{to} = F_z \cdot (R_o/F'_{zo}) \cdot (q_{Dz1} + q_{Dz2} df_z) \cdot \lambda_t \cdot \mathrm{sgn}\,V_{cx} \tag{4.E42}$$

$$D_t = D_{to} \cdot (1 + q_{Dz3}|\gamma^*| + q_{Dz4}\gamma^{*2}) \cdot \zeta_5 \tag{4.E43}$$

$$E_t = (q_{Ez1} + q_{Ez2} df_z + q_{Ez3} df_z^2)\{1 + (q_{Ez4} + q_{Ez5}\gamma^*)\frac{2}{\pi}\arctan(B_t C_t \alpha_t)\} \quad (\leq 1) \tag{4.E44}$$

$$B_r = (q_{Bz9} \cdot \lambda_{Ky\alpha}/\lambda^*_{\mu y} + q_{Bz10} B_y C_y) \cdot \zeta_6 \quad (\text{ preferred: } q_{Bz9} = 0) \tag{4.E45}$$

$$C_r = \zeta_7 \tag{4.E46}$$

$$D_r = F_z R_o \{ (q_{Dz6} + q_{Dz7} df_z) \lambda_{Mr} \zeta_2 + (q_{Dz8} + q_{Dz9} df_z) \gamma^* \lambda_{Kz\gamma} \zeta_0 +$$
$$+ (q_{Dz10} + q_{Dz11} df_z) \gamma^* |\gamma^* | \zeta_0 \} \cos' \alpha \cdot \lambda^*_{\mu y} \operatorname{sgn} V_{cx} + \zeta_8 - 1 \qquad (4.E47)$$

$$K_{z\alpha o} = D_{to} K_{y\alpha, \gamma = 0} \qquad (= \sim -\partial M_{zo}/\partial \alpha_y \ \text{at} \ \alpha_y = \gamma = 0) \quad (= C_{M\alpha}) \qquad (4.E48)$$

$$K_{z\gamma o} = F_z R_o (q_{Dz8} + q_{Dz9} df_z) \lambda_{Kz\gamma} - D_{to} K_{y\gamma o}$$
$$(= \sim \partial M_{zo}/\partial \gamma \ \text{at} \ \alpha = \gamma = 0) \quad (= C_{M\gamma}) \qquad (4.E49)$$

Longitudinal Force (combined slip)

$$F_x = G_{x\alpha} \cdot F_{xo} \qquad (4.E50)$$

$$G_{x\alpha} = \cos[C_{x\alpha} \arctan \{ B_{x\alpha} \alpha_S - E_{x\alpha} (B_{x\alpha} \alpha_S - \arctan(B_{x\alpha} \alpha_S)) \}] / G_{x\alpha o} \quad (>0) \qquad (4.E51)$$

$$G_{x\alpha o} = \cos[C_{x\alpha} \arctan \{ B_{x\alpha} S_{Hx\alpha} - E_{x\alpha} (B_{x\alpha} S_{Hx\alpha} - \arctan(B_{x\alpha} S_{Hx\alpha})) \}] \qquad (4.E52)$$

$$\alpha_S = \alpha^* + S_{Hx\alpha} \qquad (4.E53)$$

$$B_{x\alpha} = (r_{Bx1} + r_{Bx3} \gamma^{*2}) \cos[\arctan(r_{Bx2} \kappa)] \cdot \lambda_{x\alpha} \qquad (>0) \qquad (4.E54)$$

$$C_{x\alpha} = r_{Cx1} \qquad (4.E55)$$

$$E_{x\alpha} = r_{Ex1} + r_{Ex2} df_z \qquad (\le 1) \qquad (4.E56)$$

$$S_{Hx\alpha} = r_{Hx1} \qquad (4.E57)$$

Lateral Force (combined slip)

$$F_y = G_{y\kappa} \cdot F_{yo} + S_{Vy\kappa} \qquad (4.E58)$$

$$G_{y\kappa} = \cos[C_{y\kappa} \arctan \{ B_{y\kappa} \kappa_S - E_{y\kappa} (B_{y\kappa} \kappa_S - \arctan(B_{y\kappa} \kappa_S)) \}] / G_{y\kappa o} \quad (>0) \qquad (4.E59)$$

$$G_{y\kappa o} = \cos[C_{y\kappa} \arctan \{ B_{y\kappa} S_{Hy\kappa} - E_{y\kappa} (B_{y\kappa} S_{Hy\kappa} - \arctan(B_{y\kappa} S_{Hy\kappa})) \}] \qquad (4.E60)$$

$$\kappa_S = \kappa + S_{Hy\kappa} \qquad (4.E61)$$

$$B_{y\kappa} = (r_{By1} + r_{By4} \gamma^{*2}) \cos[\arctan \{ r_{By2} (\alpha^* - r_{By3}) \}] \cdot \lambda_{y\kappa} \qquad (>0) \qquad (4.E62)$$

$$C_{y\kappa} = r_{Cy1} \qquad (4.E63)$$

$$E_{y\kappa} = r_{Ey1} + r_{Ey2} df_z \qquad (\le 1) \qquad (4.E64)$$

$$S_{Hy\kappa} = r_{Hy1} + r_{Hy2} df_z \qquad (4.E65)$$

$$S_{Vy\kappa} = D_{Vy\kappa} \sin[r_{Vy5} \arctan(r_{Vy6} \kappa)] \cdot \lambda_{Vy\kappa} \qquad (4.E66)$$

$$D_{Vy\kappa} = \mu_y F_z \cdot (r_{Vy1} + r_{Vy2} df_z + r_{Vy3} \gamma^*) \cdot \cos[\arctan(r_{Vy4} \alpha^*)] \cdot \zeta_2 \qquad (4.E67)$$

Normal Load (see also Eqs.(7.45) and (9.217))

$$F_z = p_{z1} \cdot (F'_{zo}/R_o) \cdot \rho_z \cdot \lambda_{Cz} \qquad (\geq 0)$$
$$(C_{Fz} = \partial F_z/\partial \rho_z = p_{z1} \lambda_{Cz} F'_{zo}/R_o)$$

(4.E68)

Overturning Couple (see also Sec.4.3.5)

$$M_x = F_z R_o \cdot (q_{sx1} - q_{sx2}\gamma^* + q_{sx3}F_y/F'_{zo}) \cdot \lambda_{Mx}$$

(4.E69)

Rolling Resistance Moment (see also Eqs.(9.236,9.230))

$$M_y = -F_z R_o \cdot \{q_{sy1} \arctan(V_r/V_o) + q_{sy2}F_x/F'_{zo}\} \cdot \lambda_{My}$$

(4.E70)

Aligning Torque   (combined slip)

$$M_z = M'_z + M_{zr} + s \cdot F_x$$

(4.E71)

$$M'_z = -t \cdot F'_y$$

(4.E72)

$$t = t(\alpha_{t,eq}) = D_t \cos[C_t \arctan\{B_t\alpha_{t,eq} - E_t(B_t\alpha_{t,eq} - \arctan(B_t\alpha_{t,eq}))\}] \cdot \cos'\alpha$$

(4.E73)

$$F'_y = F_y - S_{Vy\kappa}$$

(4.E74)

$$M_{zr} = M_{zr}(\alpha_{r,eq}) = D_r \cos[C_r \arctan(B_r\alpha_{r,eq})]$$

(4.E75)

$$s = R_o \cdot \{s_{sz1} + s_{sz2}(F_y/F'_{zo}) + (s_{sz3} + s_{sz4}df_z)\gamma^*\} \cdot \lambda_s$$

(4.E76)

$$\alpha_{t,eq} = \sqrt{\alpha_t^2 + \left(\frac{K_{x\kappa}}{K'_{y\alpha}}\right)^2 \kappa^2} \cdot \text{sgn}(\alpha_t)$$

(4.E77)

$$\alpha_{r,eq} = \sqrt{\alpha_r^2 + \left(\frac{K_{x\kappa}}{K'_{y\alpha}}\right)^2 \kappa^2} \cdot \text{sgn}(\alpha_r)$$

(4.E78)

Note that actually $-S_{Hx}C_{F\kappa}$ should equal M_y/r_l making $\kappa=0$ at free rolling (drive torque $M_D=0$). If S_{Hx} is set equal to zero, κ vanishes at $M_D=M_y$ making $F_x=0$.

A set of parameter values have been listed in App.3 for an example tyre in connection with the *SWIFT* tyre model to be dealt with in Chapter 9. Examples of computed characteristics compared with experimentally assessed curves for both pure slip and combined slip conditions are discussed in Section 4.3.6 of this chapter, cf. Figs.4.28-32. In the next Section 4.3.3 the effect of having turn slip is modelled and some calculated characteristics have been presented for a set of hypothetical model parameters (Fig.4.19). Section 4.3.4 examines the possibility

to define the effects of conicity and ply-steer as responses to equivalent camber and slip angles. Section 4.3.5 gives a possibly better description than (4E.69) for the overturning couple of truck, car and racing tyres due to side slip and for the part due to camber that is illustrated for the case of a motorcycle tyre.

4.3.3. Extension of the Model for Turn Slip

The model described so far contains the input slip quantities side slip, longitudinal slip and wheel camber. In the present section the turn slip or (in steady state) path curvature is added which completes the description of the steady state force and moment generation properties of the tyre.

Turn slip is one of the two components which together form the spin of the tyre, cf. Fig.3.22. The turn slip is defined here as:

$$\varphi_t = -\frac{\dot{\psi}}{V_c'} = -\frac{1}{R} \tag{4.75}$$

and the total tyre spin, cf. Eq.(3.55) :

$$\varphi = -\frac{1}{V_c'}\{\dot{\psi} - (1 - \varepsilon_\gamma)\Omega \sin\gamma\} \tag{4.76}$$

with the singularity protected velocity V_c'. Again, ε_γ denotes the camber reduction factor for the camber to become comparable with turn slip. For radial-ply car tyres this reduction factor ε_γ may become as high as ca. 0.7 (for some truck tyres even slightly over 1.0) while for a motorcycle tyre the factor is expected to be close to zero like with a homogeneous solid ball, cf. discussion below Eq. (3.117).

In the previous section the effect of camber was introduced. For the side force this resulted in a horizontal and a vertical shift of the F_y vs α curves, while for the aligning torque, besides the small effect of the shifted F_y curve, the residual torque M_{zr} was added in which a contribution of camber occurs. Furthermore, changes in shape appeared to occur which were represented by the introduction of γ in factors like μ_y, E_y, $K_{y\alpha}$, B_t, D_t etc. These changes may be attributed to changes in tyre cross section and contact pressure distribution resulting from the wheel inclination angle.

These shifts and shape changes will be retained in the model extension but will be expanded to cover the complete range of spin in combination with side slip and also longitudinal slip. The spin may change from zero to $\pm\infty$ when path curvature goes to infinity and, consequently, path radius to zero (when the velocity $V_c \rightarrow 0$). Weighting functions will again be introduced to gradually reduce peak side and longitudinal forces with increasing spin. Also, cornering stiffness
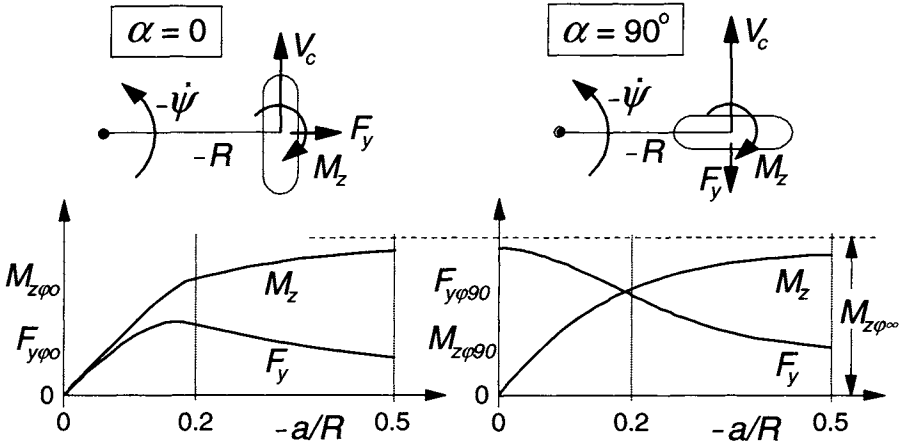
Fig. 4.18. Two basic spin force and moment diagrams.

and pneumatic trail will be subjected to such a reduction.

The theoretical findings which have been gained from the physical model of Section 3.3 presented in Fig.3.35d will be used as basis for the model development. Since these findings hold for only one value of the vertical load and zero longitudinal slip, the influence of load variations and longitudinal slip have been structured tentatively.

In Fig.4.18 for the two extreme cases of $\alpha = 0$ and $\alpha = 90°$ the courses of F_y and M_z vs $a\varphi_t = -a/R$ have been depicted. The pure spin side force characteristic shown in the left-hand diagram (at $\alpha = 0$), also indicated in the lower left diagram of Fig.3.35d, can be fabricated by sideways shifting of the side force curve belonging to zero spin (turn slip $\varphi_t = 0$ and $\gamma = 0$, upper or middle left diagram) while at the same time reducing its peak value D_y and its slope at the curve centre $K_{y\alpha}$. For this, we define the reduction functions to be substituted in the previous Eqs.(4.E22,4.E25,4.E28,4.E29). The peak side force reduction factor:

$$\zeta_2 = \cos[\arctan\{B_{y\varphi}(R_o|\varphi_t| + p_{Dy\varphi4}\sqrt{R_o|\varphi_t|})\}] \tag{4.77}$$

with sharpness factor:

$$B_{y\varphi} = p_{Dy\varphi1}(1 + p_{Dy\varphi2}df_z)\cos[\arctan(p_{Dy\varphi3}\tan\alpha)] \tag{4.78}$$

and the slope reduction factor:

$$\zeta_3 = \cos[\arctan(p_{Ky\varphi1}R_o^2\varphi_t^2)] \tag{4.79}$$

Herewith, the condition is satisfied that at $\varphi_t \to \infty$, where the wheel is steered about the vertical axis at a speed of travel equal to zero (that is: velocity of contact centre $V_c \to 0$ and path radius $R \to 0$, leading to $\zeta_2 = \zeta_3 = 0$), the side force

reduces to zero although a slip angle may theoretically still exist. Considering the upper or middle left diagram of Fig.3.35d, it seems that the sideways shift saturates at larger values of spin. To model this phenomenon, which actually says that beyond a certain negative slip angle no spin is large enough to make the side force vanish, the sine version of the magic formula is used. We have:

$$S_{Hy\varphi} = D_{Hy\varphi}\sin[C_{Hy\varphi}\arctan\{B_{Hy\varphi}R_o\varphi - E_{Hy\varphi}(B_{Hy\varphi}R_o\varphi - \arctan(B_{Hy\varphi}R_o\varphi))\}]$$

(4.80)

The shape factor $C_{Hy\varphi}$ is expected to be equal or smaller than unity. To expression (4.80) is added the shift due to ply-steer and conicity. Finally, we subtract the horizontal displacement of the point of intersection of the side force vs slip angle curve which arises due to the vertical shift of the curve (which for now is thought to be solely attributed to the camber component of spin). This leads to a total horizontal shift:

$$S_{Hy} = (p_{Hy1} + p_{Hy2}\,df_z)\cdot\lambda_{Hy} + S_{Hy\varphi} - S_{Vy\gamma}/K'_{y\alpha}$$

(4.81)

in which the vertical shift due to γ reads:

$$S_{Vy\gamma} = F_z\cdot(p_{Vy3} + p_{Vy4}df_z)\gamma^*\cdot\zeta_2\cdot\lambda_{Ky\gamma}\cdot\lambda'_{\mu y}$$

(4.82)

cf. Eq.(4.E28). The quantity $K'_{y\alpha}$ is the singularity protected cornering stiffness defined by Eq.(4.E39). Through this manipulation, the camber/spin stiffness is solely attributed to the horizontal shift of the point of intersection $S_{Hy\varphi}$, cf. Eqs.(4.88,4.89). Apparently, the factors ζ in Eq.(4.E27) now read:

$$\zeta_0 = 0$$

(4.83)

$$\zeta_4 = 1 + S_{Hy\varphi} - S_{Vy\gamma}/K'_{y\alpha}$$

(4.84)

The various factors appearing in (4.80) are defined as follows:

$$C_{Hy\varphi} = p_{Hy\varphi1} \quad (>0)$$

(4.85)

$$D_{Hy\varphi} = (p_{Hy\varphi2} + p_{Hy\varphi3}\,df_z)\cdot\text{sgn}(V_{cx})$$

(4.86)

$$E_{Hy\varphi} = p_{Hy\varphi4} \quad (\leq 1)$$

(4.87)

$$B_{Hy\varphi} = K_{yR\varphi o}/\{C_{Hy\varphi}D_{Hy\varphi}(K_{y\alpha o} + \varepsilon_K)\}$$

(4.88)

where the spin force stiffness $K_{yR\varphi o}$ is related to the camber stiffness $K_{y\gamma o}$ $(=C_{F\gamma})$ that is given by (4.E30):

$$K_{yR\varphi o} = K_{y\gamma o}/(1 - \varepsilon_\gamma) \quad (=\partial F_{yo}/\partial R_o\varphi \text{ at } \alpha = \gamma = \varphi = 0) \quad (=C_{F\varphi}/R_o)$$

(4.89)

for which we may define:

$$\varepsilon_\gamma = p_{\varepsilon\gamma\varphi1}(1 + p_{\varepsilon\gamma\varphi2}df_z)$$

(4.90)

Obviously, this parameter governs the difference of the response to camber with respect to that of turn slip.

For modelling the aligning torque, we will use as before the product of the side force and the pneumatic trail in the first term of Eqs.(4.E31,4.E71) while for the second term the residual torque will be expanded to represent large spin torque.

The middle right diagram of Fig.3.35d shows that at increasing turn slip the residual or spin torque increases while the moment due to side slip (clearly visible at $\varphi_t = 0$) diminishes. This decay is modelled by means of the weighting function ζ_5 multiplied with the pneumatic trail in Eq.(4.E43):

$$\zeta_5 = \cos[\arctan(q_{Dt\varphi 1} R_o \varphi_t)] \tag{4.91}$$

The second term of Eqs.(4.E31,4.E71), the residual torque, which in the present context may be better designated as the spin moment, is given by Eqs.(4.E36,4.E75). Its peak value D_r has an initial value due to conicity that is expected to be taken over gradually by an increasing turn slip. In (4.E47) this is accomplished by the weighting function ζ_2 (4.77). The remaining terms will be replaced by the peak spin torque $D_{r\varphi}$. This means that the ζ's appearing in (4.E47) become besides according to (4.83):

$$\zeta_8 = 1 + D_{r\varphi} \tag{4.92}$$

As observed in the middle right diagram of Fig.3.35d, the peak torque (that will be assumed to occur at a slip angle $\alpha = -S_{Hf}$ where $F_y = 0$) grows with increasing spin and finally saturates. The magic formula describes this as follows:

$$D_{r\varphi} = D_{Dr\varphi} \sin[C_{Dr\varphi} \arctan\{B_{Dr\varphi} R_o \varphi - E_{Dr\varphi}(B_{Dr\varphi} R_o \varphi - \arctan(B_{Dr\varphi} R_o \varphi))\}] \tag{4.93}$$

Its maximum value (if $C_{Dr\varphi} \geq 1$) is $D_{Dr\varphi}$. The asymptotic level of the peak spin torque is reached at $\varphi \to \infty$ or $R \to 0$, and is denoted as $M_{z\varphi\infty}$. Consequently, with the shape factor $C_{Dr\varphi}$ the maximum value is expressed by:

$$D_{Dr\varphi} = M_{z\varphi\infty} / \sin(0.5\pi C_{Dr\varphi}) \tag{4.94}$$

where the moment $M_{z\varphi\infty}$ that occurs at vanishing wheel speed and at constant turning about the vertical axis is formulated as a function of the normal load:

$$M_{z\varphi\infty} = q_{Cr\varphi 1} \mu_y R_o F_z \sqrt{F_z/F'_{zo}} \cdot \lambda_{M\varphi} \quad (>0) \tag{4.95}$$

This expression may be compared with or replaced by expression (3.117) formulated by Freudenstein (1961). The shape factors in (4.93) are assumed to be given by constant parameters:

$$C_{Dr\varphi} = q_{Dr\varphi 1} \quad (>0) \tag{4.96}$$

$$E_{Dr\varphi} = q_{Dr\varphi 2} \quad (\leq 1) \tag{4.97}$$

while

$$B_{Dr\varphi} = K_{z\gamma ro} / \{(C_{Dr\varphi} D_{Dr\varphi} + \varepsilon_r)(1 - \varepsilon_\gamma)\} \tag{4.98}$$

with $K_{z\gamma ro}$ assumed to depend on the normal load as follows:

$$K_{z\gamma ro} = F_z R_o (q_{Dz8} + q_{Dz9} df_z) \lambda_{Kz\gamma} \tag{4.99}$$

As has been indicated with Eq.(4.E49) we have now for the camber moment stiffness

$$K_{z\gamma o} = K_{z\gamma ro} - D_{to} K_{y\gamma o} \quad (= C_{M\gamma}) \tag{4.100}$$

and consequently for the moment stiffness against spin:

$$K_{zR\varphi o} = K_{z\gamma o} / (1 - \varepsilon_\gamma) \quad (= C_{M\varphi} / R_o) \tag{4.101}$$

Now that the formulae for the peak of the spin torque $D_{r\varphi}$ has been developed, we must consider the remaining course of M_{zr} with the slip angle α. For this, Eq.(4.E36) is employed. According to the middle right diagram of Fig.3.35d the curves become flatter as the spin increases. Logically, for $\varphi \to \infty$ the moment should become independent of the slip angle. The sharpness is controlled by the factor B_r which we let gradually decrease to zero with increasing spin. For this, we introduce in Eq.(4.E45) the weighting function:

$$\zeta_6 = \cos[\arctan(q_{Br\varphi 1} R_o \varphi)] \tag{4.102}$$

The factor C_r controls the asymptotic level which corresponds to the torque at $\alpha = 90°$. In that situation the turn slip $\varphi_t = -\dot{\psi}/|V_{cy}| = 1/R$ which corresponds to the definition given by Eq.(4.76). The moment $M_{z\varphi 90}$ that is generated when the wheel moves at $\alpha = 90°$, increases with increasing curvature $1/R$ up to its maximum value that is attained at $R = 0$ and equals $M_{z\varphi\infty}$. We use the formula:

$$M_{z\varphi 90} = M_{z\varphi\infty} \cdot \frac{2}{\pi} \cdot \arctan(q_{Cr\varphi 2} R_o |\varphi_t|) \cdot G_{y\kappa}(\kappa) \tag{4.103}$$

with parameter $q_{Cr\varphi 2}$. This quantity may be difficult to assess experimentally; the value 0.1 is expected to be a reasonable estimate. (In any case, the argument of (4.104) should remain < 1.) This moment at $90°$ is multiplied with the weighting function $G_{y\kappa}$ (4.E59) to account for the attenuation through the action of longitudinal slip.

We obtain for the factor $\zeta_7 = C_r$ in Eq.(4.E46) using (4.E36) with $|\alpha_r| \to \infty$:

$$\zeta_7 = \frac{2}{\pi} \cdot \arccos[M_{z\varphi 90} / (|D_{r\varphi}| + \varepsilon_r)] \tag{4.104}$$

Finally, we must take care of the weighting function ζ_1 which is introduced in the expressions (4.E12,4.E18) for F_x to let the longitudinal force diminish with increasing spin. We define:

$$\zeta_1 = \cos[\arctan(B_{x\varphi} R_o \varphi)] \tag{4.105}$$

with

$$B_{x\varphi} = p_{Dx\varphi1}(1 + p_{Dx\varphi2} df_z)\cos[\arctan(p_{Dx\varphi3}\kappa)] \qquad (4.106)$$

With the factors ζ_0, ζ_1,......ζ_8 determined and substituted in the equations (4.E9-78) the description of the steady-state force and moment generation has been completed. To show that the formulae produce qualitatively correct results, a collection of computed curves have been presented in the diagrams of Fig.4.19. In Table 4.2 the values of the model parameters have been listed. The diagrams show that the formulae are perfectly capable to at least qualitatively approximate the curves that have been computed with the brush simulation model of Chapter 3 (cf. Fig.3.35). It has not been attempted to find a best fit for the parameters.

Table 4.2. *Magic Formula* hypothetical parameter values. Parameters that govern the influence of longitudinal slip and changes in vertical load have been given the tentative value zero

$F_z = 3000N \qquad F_{zo} = 3000N \qquad R_o = 0.3m \qquad R_e = R_o \qquad (a = 0.1m)$

$p_{Cx1} = 1.65$	$p_{Dx1} = 1$	$p_{Dx2} = 0$	$p_{Ex1} = -0.5$	$p_{Ex2} = 0$	$p_{Ex3} = 0$	$p_{Ex4} = 0$
$p_{Kx1} = 12$	$p_{Kx2} = 10$	$p_{Kx3} = -0.6$	$p_{Hx1} = 0$	$p_{Hx2} = 0$	$p_{Vx1} = 0$	$p_{Vx2} = 0$
$p_{Cy1} = 1.3$	$p_{Dy1} = 1$	$p_{Dy2} = 0$	$p_{Dy3} = 0$			
$p_{Ey1} = -1$	$p_{Ey2} = 0$	$p_{Ey3} = 0$	$p_{Ey4} = 0$			
$p_{Ky1} = 10$	$p_{Ky2} = 1.5$	$p_{Ky3} = 0$	$p_{Ky4} = 2$	$p_{Ky5} = 0$	$p_{Ky6} = 2.5$	$p_{Ky7} = 0$
$p_{Hy1} = 0$	$p_{Hy2} = 0$	$p_{Vy1} = 0$	$p_{Vy2} = 0$	$p_{Vy3} = 0.15$	$p_{Vy4} = 0$	

$q_{Bz1} = 6$	$q_{Bz2} = -4$	$q_{Bz3} = 0.6$	$q_{Bz4} = 0$	$q_{Bz5} = 0$	$q_{Bz9} = 0$	$q_{Bz10} = 0.7$
$q_{Cz1} = 1.05$	$q_{Dz1} = 0.12$	$q_{Dz2} = -0.03$	$q_{Dz3} = 0$	$q_{Dz4} = -1$	$q_{Dz6} = 0$	$q_{Dz7} = 0$
$q_{Dz8} = 0.6$	$q_{Dz9} = 0.2$	$q_{Dz10} = 0$	$q_{Dz11} = 0$	$q_{Ez1} = -10$	$q_{Ez2} = 0$	$q_{Ez3} = 0$
$q_{Ez4} = 0$	$q_{Ez5} = 0$	$q_{Hz1} = 0$	$q_{Hz2} = 0$	$q_{Hz3} = 0$	$q_{Hz4} = 0$	

$r_{Bx1} = 5$	$r_{Bx2} = 8$	$r_{Bx3} = 0$	$r_{Cx1} = 1$	$r_{Hx1} = 0$		
$r_{By1} = 7$	$r_{By2} = 2.5$	$r_{By3} = 0$	$r_{By4} = 0$	$r_{Cy1} = 1$	$r_{Hy1} = 0.02$	
$r_{Vy1} = 0$	$r_{Vy2} = 0$	$r_{Vy3} = -0.2$	$r_{Vy4} = 14$	$r_{Vy5} = 1.9$	$r_{Vy6} = 10$	
$s_{sz1} = 0$	$s_{sz2} = -0.1$	$s_{sz3} = -1.0$	$s_{sz4} = 0$			

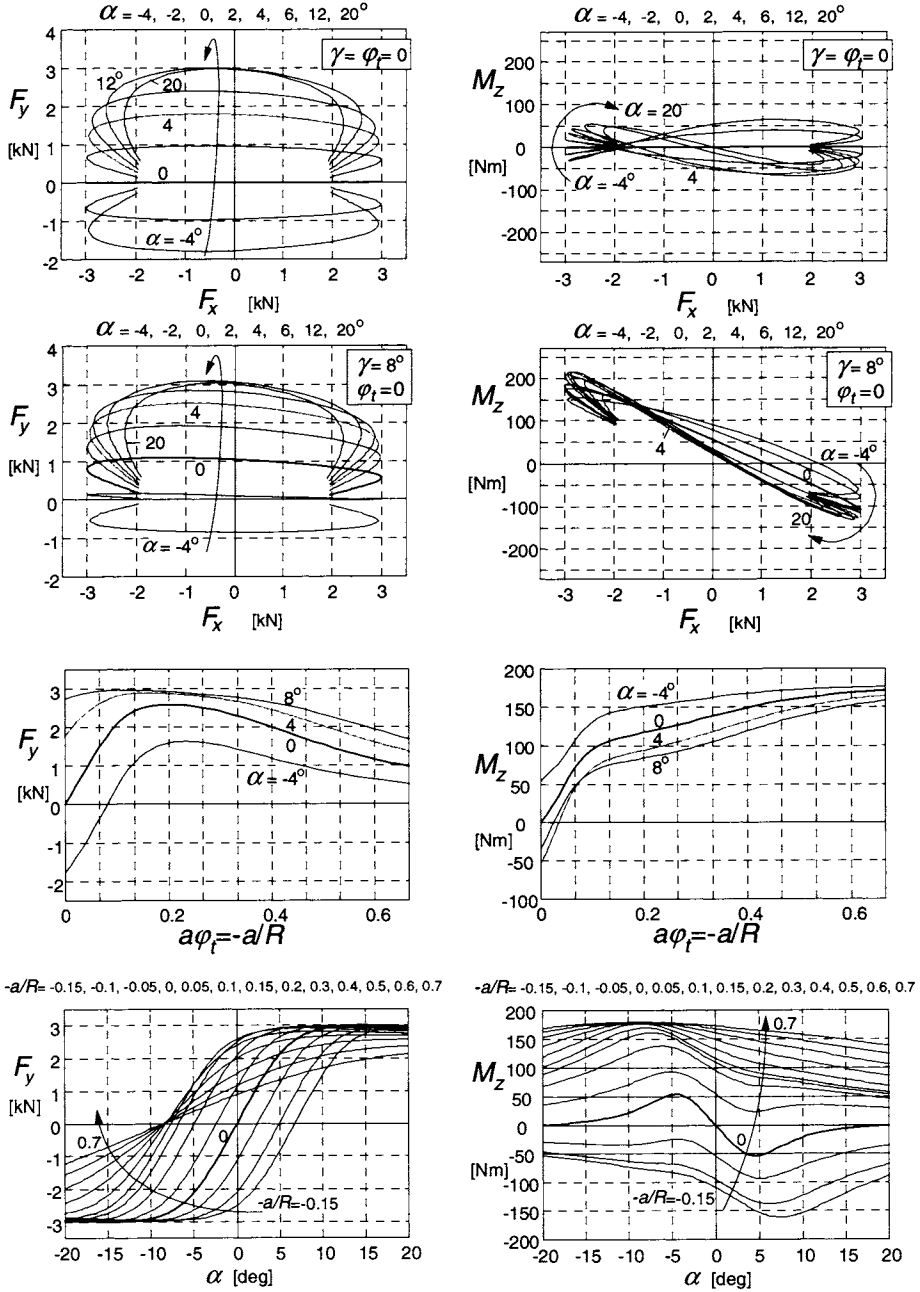|					
$p_{Dx\varphi1} = 0.4$	$p_{Dx\varphi2,3} = 0$	$p_{Ky\varphi1} = 1$	$p_{Dy\varphi1} = 0.4$	$p_{Dy\varphi2} = 0$	$p_{Dy\varphi3,4} = 0$
$p_{Hy\varphi1} = 1$	$p_{Hy\varphi2} = 0.15$	$p_{Hy\varphi3} = 0$	$p_{Hy\varphi4} = -4$	$p_{\varepsilon y\varphi1} = 0$	$p_{\varepsilon y\varphi2} = 0$
$q_{Dt\varphi1} = 10$	$q_{Cr\varphi1} = 0.2$	$q_{Cr\varphi2} = 0.1$	$q_{Br\varphi1} = 0.1$	$q_{Dr\varphi1} = 1$	$q_{Dr\varphi2} = -1.5$

Fig. 4.19. *Magic Formula* results for steady-state response of forces $F_{x,y}$ and moment M_z to slip angle α, slip ratio κ, camber angle γ and path curvature $\varphi_t = -1/R$.

4.3.4. Ply-Steer and Conicity

In the formulae for the side force F_y and the aligning torque M_z, the vertical shift S_{Vy}, the horizontal shift S_{Hy} and the residual torque peak value D_r contain terms which produce the initial values of side force and aligning torque that occur at straight ahead running (at $\alpha = 0$). These initial values are known to be the result of conicity and ply-steer, which are connected with non-symmetry of the tyre construction. These two possible sources result in markedly different behaviour of the tyre when, at geometrically zero side slip, the tyre is rolled forwards or backwards. If we would have a tyre that exhibits ply-steer but no conicity the generated side force will point to the opposite direction when the wheel is changed from forward to backward rolling. This would also be the case when on a test rig the wheel moves at a small steer angle ψ and the road surface motion is changed from backward to forward. For that reason, ply-steer is sometimes referred to as pseudo side slip. If on the other hand the tyre would show pure conicity, the side force will remain pointing in the same direction when the wheel is rolled in the opposite direction. That behaviour is similar to that of a cambered wheel, which explains the term: pseudo camber. In Fig.4.20 for the different cases the diagrams for the side force variation resulting from yaw angle variations have been depicted. The curved or scewed foot prints of the tyre that due to non-symmetric construction of carcass and belt would arise on a zero friction surface explains the resulting characteristics. Definitions of conicity and ply-steer follow from the forces found at zero steer angle ψ.

   The deformations of the tyre rolling on a friction surface resemble those that would occur with a tyre (free of conicity and ply-steer) that rolls at a small
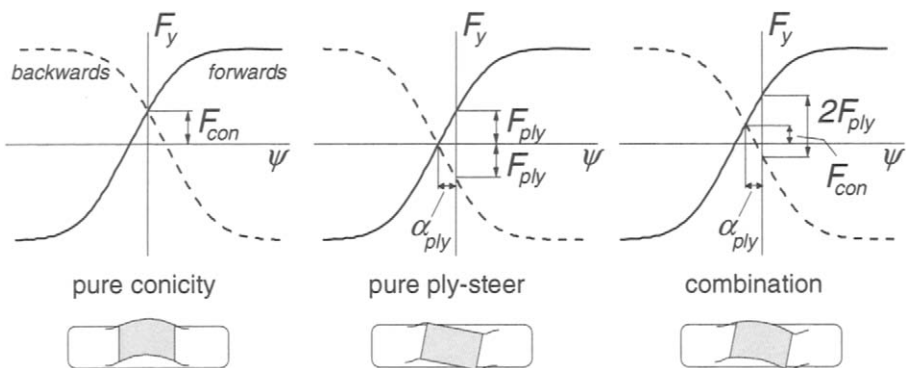

Fig. 4.20. Side force vs steer angle characteristics at forward and backward rolling showing the cases of pure conicity, pure ply-steer and a combination of both situations. Below, the associated foot prints on a frictionless surface have been depicted.

camber and side slip angle respectively. It is therefore tempting to assume that in these comparable cases the moment M_z and the force F_y respond at the same rate which would mean that the associated pneumatic trails are equal for ply-steer and side slip and for conicity and camber. The assumption is partly supported by an extensive experimental investigation of Lee (2000), which assessed a strong linear correlation between conicity and the difference between slip angles where F_y and M_z become equal to zero. In Fig.4.21 this difference is designated as δ_o. Lee found that at $\delta_o = 0$ conicity is almost zero. This means that for vanishing conicity the remaining ply-steer produces a moment that is approximately equal to minus the pneumatic trail for side slip times the side force. With the introduction of the (small) equivalent slip angle α_{ply} we have:

$$M_{ply} \approx -C_{M\alpha}\alpha_{ply} \quad \text{with} \quad C_{M\alpha} = tC_{F\alpha} \tag{4.107}$$

and

$$F_{ply} \approx C_{F\alpha}\alpha_{ply} \tag{4.108}$$

Also according to Lee, the residual torque at zero side force, M_{zr0} in Fig.4.21, is strongly correlated with δ_o and thus with conicity. We find from the diagram:

$$M_{zr0} \approx C_{M\alpha}\delta_o \tag{4.109}$$

If we may further assume that for the conicity force and moment a similar correspondence with camber response exists we would have after introducing an equivalent camber angle γ_{con}:

$$M_{con} \approx C_{M\gamma}\gamma_{con} \quad \text{with} \quad C_{M\gamma} = t_\gamma C_{F\gamma} \tag{4.110}$$

where t_γ (>0) represents the distance of the point of application of the resulting camber thrust in front of the contact centre (that is: negative trail). The conicity force becomes:
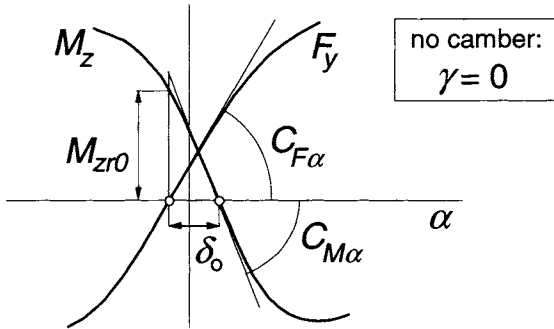

Fig. 4.21. The situation near zero slip angle, force and moment due to conicity and ply-steer.

$$F_{con} \approx C_{F\gamma}\gamma_{con} \tag{4.111}$$

With these assumptions it is possible to estimate the contributions of ply-steer and conicity in the initial values of side force and aligning torque (at $\alpha = \gamma = 0$) from a set of tyre parameters that belongs to one direction of rolling.

This enables the vehicle modeller to switch easily from the set of parameter values of the tyre model that runs on the left-hand wheels of a car to the set for the right-hand wheels. To accomplish this, the equivalent camber parts of the left-hand tyre model must be changed in sign for both the aligning moment and the side force to make the model suitable for the right-hand tyre. Also, it is then easy to omit e.g. all conicity contributions which were originally present in the tyre from which the parameters have been assessed through the fitting process.

To develop the theory, we will first consider the case of a tyre without ply-steer and conicity and study the situation when a camber angle is applied. This condition is reflected by the diagram of Fig.4.22. Considering the relations entered in this figure, we may write for the distance δ_γ

$$\delta_\gamma = \left(\frac{C_{M\gamma}}{C_{M\alpha}} + \frac{C_{F\gamma}}{C_{F\alpha}} \right) \gamma \tag{4.112}$$

and consequently we can find the camber angle γ from the distance δ_γ. In a similar fashion the conicity will be assessed in terms of the equivalent camber angle and after that, the part attributed to ply-steer can be determined and expressed in terms of the equivalent slip angle. Figure 4.23 illustrates the conversion to equivalent angles. We find similar to the inverse of (4.112)

$$\gamma_{con} = \frac{\delta_o}{\dfrac{C_{M\gamma}}{C_{M\alpha}} + \dfrac{C_{F\gamma}}{C_{F\alpha}}} \tag{4.113}$$
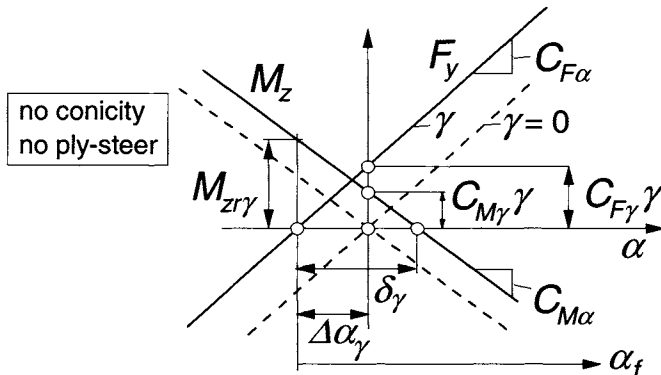

Fig. 4.22. Characteristics of a tyre without ply-steer or conicity near the origin at $\alpha = 0$, with and without camber.
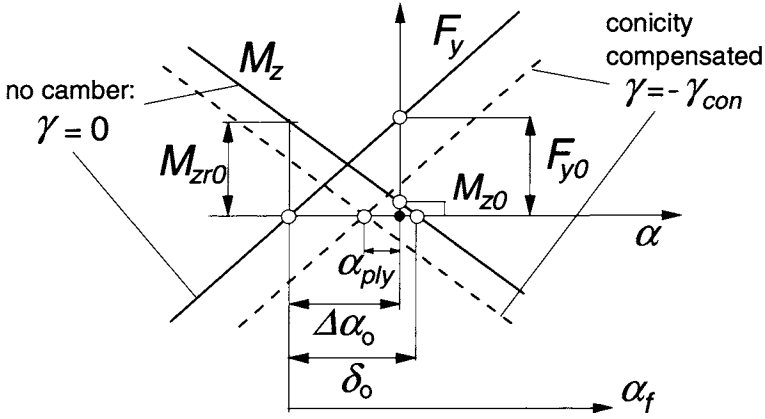
Fig. 4.23. Characteristics of a tyre with ply-steer and conicity showing conversion to equivalent camber and slip angle.

The equivalent slip angle can now be obtained from:

$$\alpha_{ply} = \Delta\alpha_o - \frac{C_{F\gamma}}{C_{F\alpha}}\gamma_{con} \tag{4.114}$$

The four slip and camber stiffnesses are available from Eqs.(4.E25,4.E30,4.E48,4.E49). The sign of the forward velocity has been properly introduced.

The next thing we have to do is expressing δ_o and $\Delta\alpha_o$ in terms of the shifts and the initial residual torque as defined in Section 4.3.2. We obtain with (4.E38):

$$\Delta\alpha_o = S_{Hf(\gamma=\varphi=0)} \tag{4.115}$$

and from (4.109) and Fig.4.23:

$$\delta_o = \frac{F_{y0}}{C_{F\alpha}} + \frac{M_{z0}}{C_{M\alpha}} = M_{zr0}/C_{M\alpha} \tag{4.116}$$

with $C_{M\alpha}$ according to Eq.(4.E48) and the initial residual torque from (4.E47):

$$M_{zr0} = D_{ro} = F_z R_o (q_{Dz6} + q_{Dz7} df_z) \cdot \lambda_{Mr} \tag{4.117}$$

Finally,the initial side force and torque are to be removed from the equations by putting the parameters p_{Hy1}, p_{Hy2}, p_{Vy1}, p_{Vy2}, q_{Dz6} and q_{Dz7} or the scaling factors λ_{Hy}, λ_{Vy} and λ_{Mr} equal to zero and by replacing in Eqs.(4.E20,4.E37) the original side slip input variable $\alpha^* = \tan\alpha \cdot \mathrm{sgn} V_x$ by its effective value:

$$\alpha_{eff}^* = (\tan\alpha + \alpha_{ply})\,\mathrm{sgn}\,V_x \tag{4.118}$$
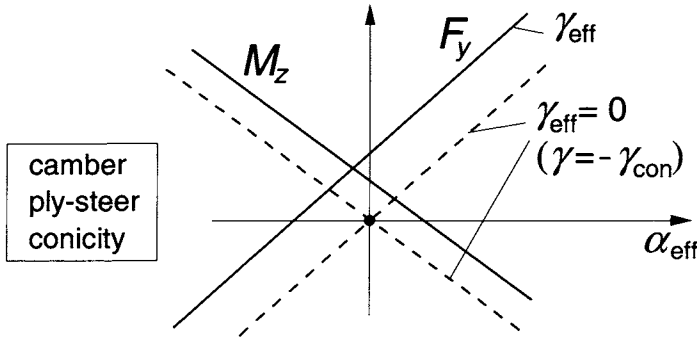
Fig. 4.24. The final diagram with effective side slip and camber variables.

and in Eqs.(4.E27,4.E28,4.E47) the original camber $\gamma^* = \sin\gamma$ by the effective total camber:

$$\gamma_{eff}^* = \sin(\gamma + \gamma_{con}) \qquad (4.119)$$

where it should be realised that both α_{ply} and γ_{con} are small quantities. The resulting diagram of Fig.4.24 shows characteristics that pass through the origin when the effective camber angle is equal to zero. For the tyre running on the other side of the vehicle the same model can be used but with γ_{con} in (4.119) changed in sign.

The theory above is based on considerations near the origin of the side force and aligning torque vs slip angle diagrams. The introduction of effective slip and camber angles may, however, give rise to slight changes in peak levels of the side force and probably also of the aligning torque. For the former, the situation may be repaired by moving the force characteristic in a direction parallel to the tangent at $F_y = 0$ resulting in an additional vertical shift:

$$\Delta S_{Vy} = F_z \cdot \{(p_{Vy1} + p_{Vy2}\, df_z) - (p_{Vy3} + p_{Vy4}\, df_z)\gamma_{eff}\} \qquad (4.120)$$

and an associated additional horizontal shift:

$$\Delta S_{Hy} = -\Delta S_{Vy} / K'_{y\alpha} \qquad (4.121)$$

Tyre Pull

If identical tyres would be fitted on the front axle of an automobile but with the conicity forces pointing in the same direction, and the vehicle moves along a straight line (that is: side forces are equal to zero) a steering torque must be applied that opposes the residual torques M_{zr0} generated by the front tyres (Fig.4.21). This is actually only approximately true because we may neglect the trails connected with ply-steer and conicity with respect to the vehicle wheel

base. (In reality we have a small couple acting on the car exerted by the equal but opposite side forces front and rear which counteract the small, mainly conicity, torques front and rear.) The phenomenon that a steer torque must be applied when moving straight ahead is called: tyre or vehicle pull. If the steering wheel would be released, the vehicle will deviate from its straight path.

If on the right-hand wheel a tyre is mounted that is identical with the left-hand tyre one would actually expect that the conicity forces are directed in opposite directions and neutralise each other (as will occur also with the moments). This is because of the observation that one might compare the condition on the right-hand side with an identical tyre rolling backwards with respect to condition of the left-hand tyre. In contrast, the ply-steer forces of the left and right tyres act in the same direction but are compensated by side forces that arise through a small slip angle of the whole vehicle.

If the ply-steer angles front and rear are not the same, a small steer angle of the front wheels equal to the difference of the ply-steer slip angles front and rear is required for the vehicle to run straight ahead. The whole vehicle will run at a slip angle equal to that of the rear wheels.

4.3.5. The Overturning Couple

The overturning couple is especially important to investigate the vehicle roll-over occurrence and the curving behaviour of a motorcycle. In moderate conditions Eq.(4.E69) may often be sufficient to model the overturning moment. In the present section we will study cases that require more elaborate modelling.
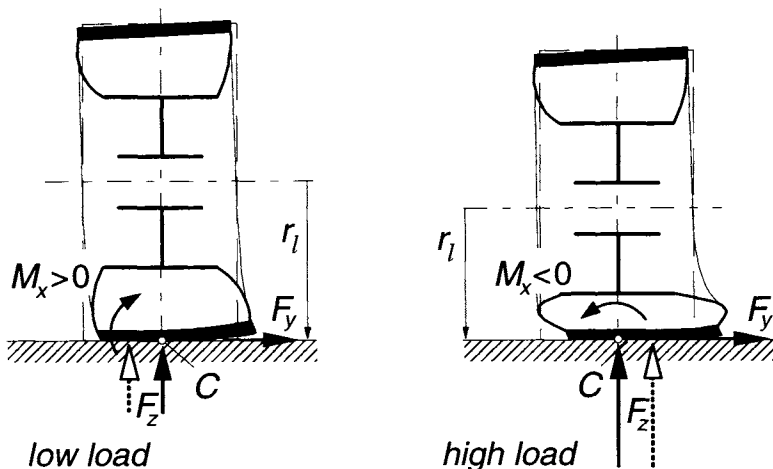

Fig. 4.25. Tyre at low load and at high load subjected to side slip giving rise to an overturning couple that may be of opposite sign.

Due to Side Slip

Experience with measuring truck tyres, racing tyres and passenger car tyres shows that a positive overturning couple arises especially at low vertical loads as a response to positive side slip (situation depicted in Fig.4.25) while camber remains zero. This is probably in contrast to the behaviour of narrow passenger car or motorcycle tyres where due to the lateral deflection connected with the side force F_y, the point of application of the resultant vertical force F_z moves in the direction of the side force and as a result generates a negative couple M_x. The observation that a tyre may show a positive moment is expected to be connected with the belt that is stiff in torsion in the contact zone. This high stiffness opposes the flattening of the belt to remain in contact with the road when the belt is tilted through the action of the side force. This will especially be true when the contact patch is short, that is: at low load. As a result, the resultant vertical force vector will move more towards the edge away from the side force which causes the contact pressure to become relatively high on that side of the contact patch thereby enabling the overturning couple to become positive. At higher loads the middle portion of the belt contact range will show less resistance to remain horizontal and the overturning couple may turn to the more common negative values. It is of importance to note that the positive overturning couple at low loads and the ensuing sign change is observed to occur when measurements are conducted on e.g. a flat plank or flat trac machine where the axle height is recorded accurately and in the processing stage proper account is given to the standard definition of the overturning couple, that is the moment about the line of intersection of wheel centre plane and ground plane. If the change in loaded radius is disregarded as is often done in past practice when measuring with over the road test vehicles, the positive part and the connected sign change is not observed. Consequently, it is of crucial importance that the tyre test engineer and the vehicle dynamicist take care of employing, at least, the same definition for the overturning couple.

The phenomenon may in some way be connected with the negative camber stiffness that is observed to occur with some type of tyres also especially at low loads turning to positive at higher loads. The negative camber force generally changes to positive values when the camber angle becomes sufficiently large. At moderate loads this also appears to happen with the overturning couple changing from positive to negative values at larger slip angles, that is: at higher side forces. The overturning couple response to wheel camber is always negative as might be expected. Obviously, the associated camber moment stiffness to be defined as $C_{M x \gamma} = -\partial M_x / \partial \gamma$ at zero camber is positive.
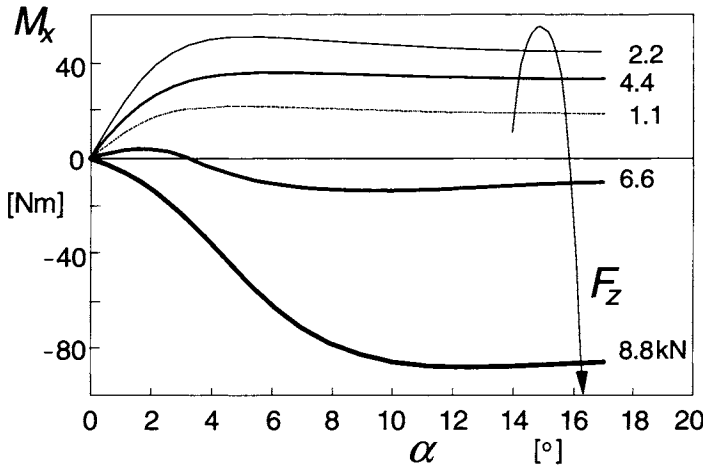
Fig. 4.26. Overturning couple calculated with formulae (4.122-124), cf. Fig.4.30 for similar measured characteristics.

To model such a sign changing situation, the overturning couple response to side slip of the wheel is taken as an example. We will use a formula that is established by adding two functions:

$$M_x = -F_z(y_1 + y_2)$$ (4.122)

with the two contributions to the moment arm:

$$y_1 = R_o q_{x1} \frac{F_y}{F_{zo}}$$ (4.123)

(4.124)

$$y_2 = -R_o q_{x2} \cos\{q_{x3} \arctan(q_{x4} F_z/F_{zo})^2\} \cdot \sin\{q_{x5} \arctan(q_{x6} F_y/F_{zo})\}$$

The first term y_1 increases with the side force. The second term y_2 grows, at least initially, with $-F_y$ and decays with vertical load F_z. For the parameter values listed in Table 4.3, also containing assumed parameters for the side force characteristic, Eqs.(4.E19-26), the overturning couple has been calculated. Figure 4.26 shows the resulting curves. The same tendencies have been found to occur both with truck tyres and passenger car tyres. For the latter, we may refer to the diagram given in Fig.4.30. The same figure, which has been reproduced from the dissertation of Van der Jagt (2000), contains the diagram showing the decrease of the loaded radius with slip angle. This information is needed to assess the moment about the longitudinal axis through the wheel centre. In Chapter 9 a formula is given which assumes that the decrease of the loaded radius is proportional to the squares of the lateral and the longitudinal deflections of the carcass, cf. Eq.(9.222). Experiments indicate that also the tyre vertical

stiffness is affected by horizontal tyre forces, cf. Reimpell (1986), Eq.(9.217).

Table 4.3. Parameter values for overturning couple computation, cf. Eqs.(4.120-122)

$F_{zo}=4.4\,\text{kN}$	$R_o = 0.3\,\text{m}$				
$\mu_y = 1$	$C_y = 1.4$	$E_y = -1$	$p_{Ky1} = 20$	$p_{Ky2} = 1.5$	$p_{Ky4} = 2$
$q_{x1} = 0.042$	$q_{x2} = 0.56$	$q_{x3} = 0.955$	$q_{x4} = 2.35$	$q_{x5} = 1.25$	$q_{x6} = 0.46$

Due to Camber

The second case to be dealt with concerns the motorcycle tyre. A special problem can be identified that concerns the possibly very large wheel inclination angle. Similar situations may be encountered with a car tyre when examining the roll-over event or when the wheel runs over a locally steep transverse slope. In these cases, the geometry of the cross section of the tyre with its finite width becomes of importance and is largely responsible for the overturning couple that arises as

Fig. 4.27. The motorcycle wheel at very large camber angle γ. Two alternative approaches to define the contact centre C and the associated 'loaded radius' r_l and as a consequence the overturning couple M_x. Instead of the circle, the actual section contour may be taken.

a result of the wheel inclination angle with respect to the road surface.

In Fig.4.27 the configuration at very large camber of a motorcycle wheel has been depicted. For simplicity, the tyre cross section has been assumed to be purely circular. Alternatively, one may take an ellipse (cf. Fig.7.14). Of course, if instead of relying on a possibly less precise measurement, the overturning couple is to be derived from a calculation where the location of the point of application of the normal force and its distance to the line of intersection (i.e. to point C) which is the moment arm, is of crucial importance, the actual measured cross section contour of the undeformed tyre, free radius versus distance to wheel centre plan $r_{yo}(y_{co})$, should be utilised. Note that at the point of contact with the not yet deformed tyre we have: d r_{yo}/d $y_{co}= -\tan\gamma$. As a consequence of the definition of the point of intersection or contact centre C which is located on the line of intersection of the wheel centre plane and the road plane, the loaded radius r_l which by definition is equal to the distance between wheel centre and contact centre, may become excessively large when the camber angle becomes large.

Although still perfectly correct, this standard definition may seem less attractive and one might want to choose for an alternative approach. Two possible alternatives have been indicated in Fig.4.27. The first one employs a value for the loaded radius r_l' that remains equal to the value that holds for the upright wheel: r_{lo} which is equal to the free radius r_o minus the normal deflection ρ_z. It should then be realised that a concurrent (slight) rise $-w'$ of the effective road plane may not be negligible. This method to acquire the overturning couple M_x' corresponds to the practical procedure often employed when measuring on the road where the actual height of the wheel centre above the road surface is not measured. The second alternative is possibly the physically most realistic one. It defines a contact centre located C'' above the lowest point of the undeformed tyre. A drawback is that an effective wheel plane has to be defined in the vehicle dynamic model that is shifted with respect to the wheel centre plane over a distance y_c.

It turns out that the overturning couples that would act about the three possible virtual contact centres defined above, become quite different from each other although the moment about the longitudinal axis through the wheel centre remains, of course, the same. We find successively if the resultant normal force is assumed to act along a line that passes through the lowest point of the (assumedly circular) tyre cross section and a through F_y with lateral compliance induced additional shift is disregarded:

1. *Standard definition, using C* (for general contour and for circular section):

$$r_l = r_{yo} + y_{co}\tan\gamma - \rho_z/\cos\gamma = r_o - r_c + (r_c - \rho_z)/\cos\gamma \qquad (4.125)$$

$$M_x = -F_z(y_{co}/\cos\gamma - \rho_z\tan\gamma) = -F_z(r_c - \rho_z)\tan\gamma \qquad (4.126)$$

2. *Practical definition, using* C':

$$r_l' = r_{lo} = r_o - \rho_z \qquad\qquad (4.127)$$

$$M_x' = -F_z(r_c - \rho_z)\sin\gamma + F_y w' \qquad\qquad (4.128)$$

$$w' = -(r_c - \rho_z)(1 - \cos\gamma) \qquad\qquad (4.129)$$

3. *Physically more realistic definition, using* C'':

$$r_l'' = r_y = r_o - r_c + (r_c - \rho_z)\cos\gamma \qquad\qquad (4.130)$$

$$M_x'' = 0 \qquad\qquad (4.131)$$

$$y_c = (r_c - \rho_z)\sin\gamma \qquad\qquad (4.132)$$

The forces act in the points C, C' and C'' respectively.

The overturning couple M_x according to the standard definition (4.126) is directly responsible for the lean angle of the motorcycle in a steady turn to become larger than what would be expected according to the ratio of centrifugal force and vehicle weight. In the practical definition it would be the combination of M_x' and the effective road surface rise w' that causes the increase in roll angle, while with the third definition it would be due to the lateral shift y_c of the virtual wheel plane.

Irrespective of the definition employed, it must be clear how the measured data have been processed and converted from the wheel axle system of axes (where in general the forces are measured) to the road and line of intersection based axes system. An additional conversion may be necessary to suit the requirements of the vehicle dynamicist. It may be realised that with respect to the standard definition of the loaded radius r_l, Eq.(4.125), the effective rolling radius r_e follows a quite different course. Also at large camber angles r_e will remain close to the radius $r_l'' = r_y$ defined by (4.130) and shown in Fig.4.27.

To account for the effect of the lateral tyre deflection and through that the change in vertical pressure distribution, the part of M_x attributed to wheel camber and defined by one of the above or similar expressions, should be extended with the part of the overturning couple described by Eqs.(4.122-124) or, if appropriate, by a simpler version of that.

Note on the Aligning Torque at Large Camber

It may be of interest to be aware of another unexpected phenomenon that arises at large camber angles. One might make a mistake when deriving the aligning torque from the wheel axle oriented measured forces and moments. If these latter quantities are denoted with an additional subscript a the aligning torque is obtained from the moment equilibrium about the vertical axis as follows (cf.

Fig.4.27):

$$M_z = M_{za}\cos\gamma + M_{ya}\sin\gamma - F_{xa}r\sin\gamma \qquad (4.133)$$

or alternatively from the moment equilibrium about the wheel radius:

$$M_z = M_y\tan\gamma + M_{za}/\cos\gamma \qquad (4.134)$$

If the fact is not recognised that at camber a longitudinal force F_x is generated even at free rolling where M_{ya} is zero or very small, and consequently, F_{xa} is disregarded in Eq.(4.133), the calculated aligning torque is incorrect. In (4.134) the rolling resistance moment M_y may not be negligible for a cambered wheel running at a side slip angle. Then, the relatively stiff belt may be axially deformed in an asymmetric way. This may explain that experiments tend to indicate that the through camber generated F_x is virtually independent of the slip angle.

4.3.6. Comparison with Experimental Data for a Car and a Truck Tyre

In Figs. 4.28,4.29 and 4.31,4.32 the computed and measured characteristics of a 195/65 R15 car tyre (on the road with Delft Tyre Test Trailer, averaged over two slip angle and brake pressure sweep cycles) and a 315/80 R22.5 truck tyre (on Calspan flat track test stand) have been presented. In general, it is observed that a good agreement between computed and measured curves can be achieved with the model. An exception is the attempt to (physically) describe the measured course of the aligning torque at braking. The diagrams concerned, in Figs.4.29 and 4.32, show a rather unpredictable variation of the moment while the brake pressure is increased until wheel lock is reached. This is assumedly due to the large direct contribution of the braking force times the moment arm. This distance between the line of action of F_x and the wheel centre plane is suspected to vary due to local road camber variations and possibly tyre non-uniformities while the tyre rolls.

Figure 4.30 presents the overturning couple and the loaded radius for a passenger car tyre as reported by Van der Jagt (2000) and measured with the Ford MTS Flat Trac III tyre testing facility. One may compare the measured characteristics with the calculated curves shown in Fig.4.26 obtained from Eqs. (4.122-124) with hypothetical (not optimised) parameter values (Table 4.3).
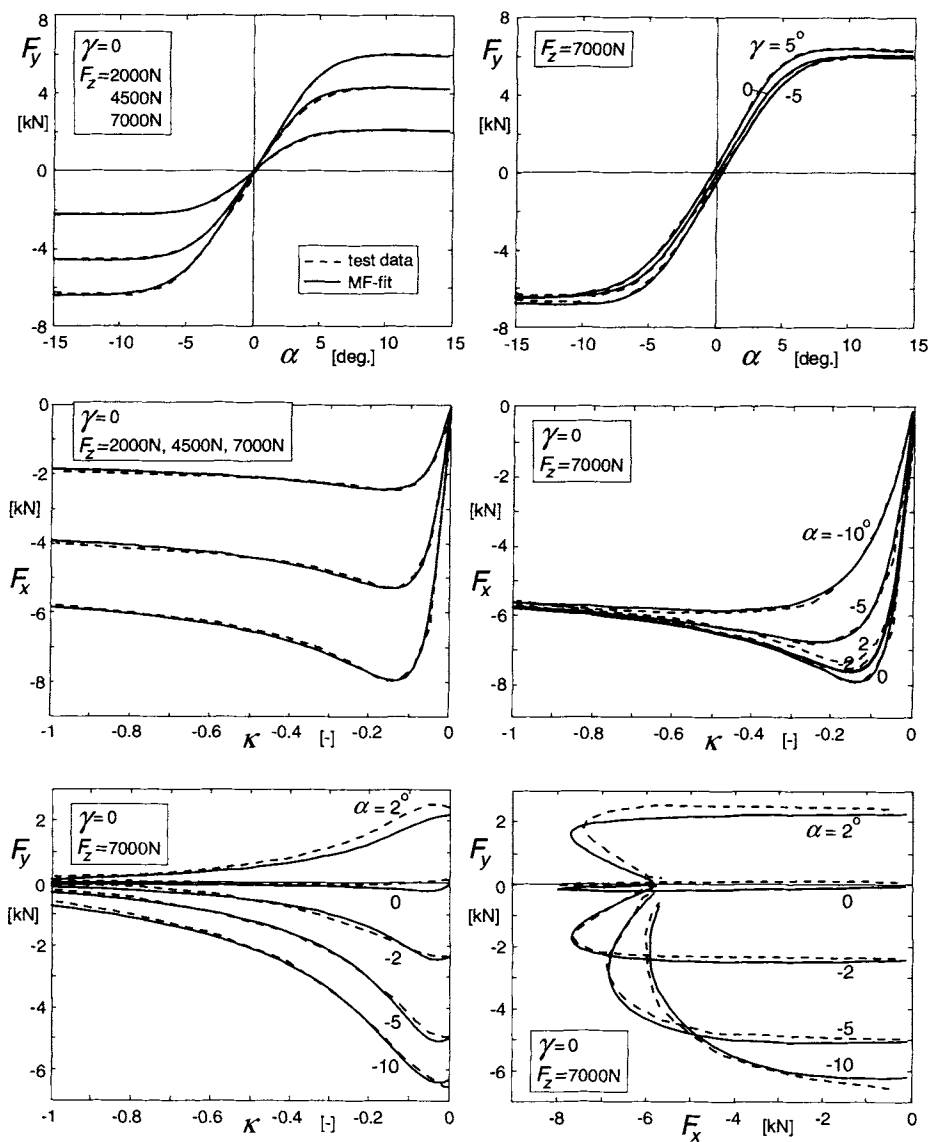
Fig. 4.28. Force characteristics of a 195/65 R15 car tyre. *Magic Formula* computed results compared with data from measurements (dotted curves) conducted with the Delft Tyre Test Trailer (2000).
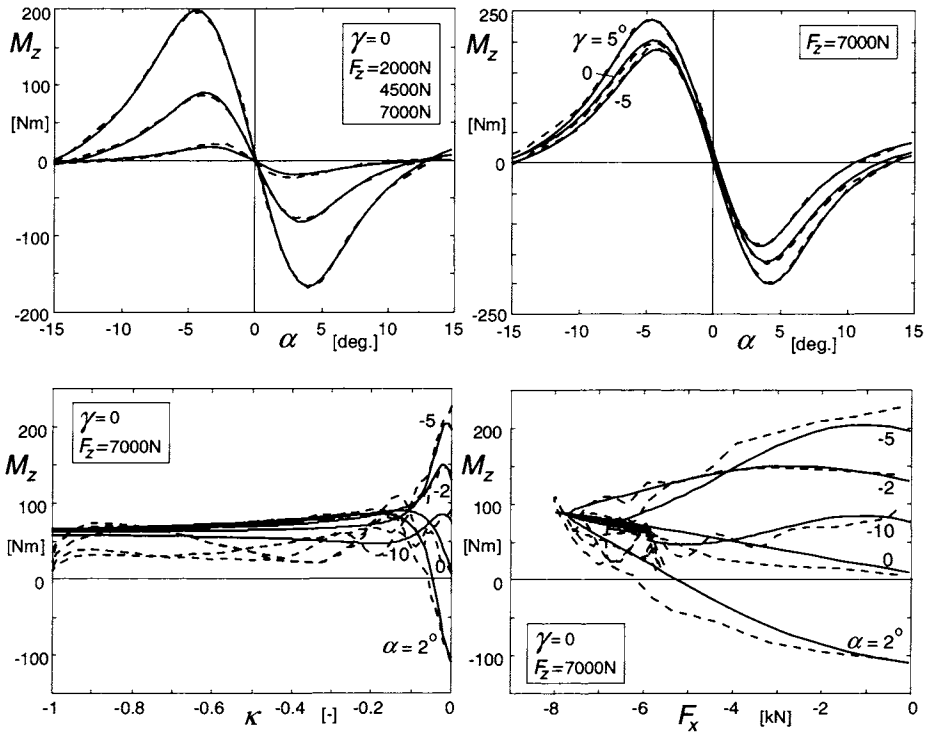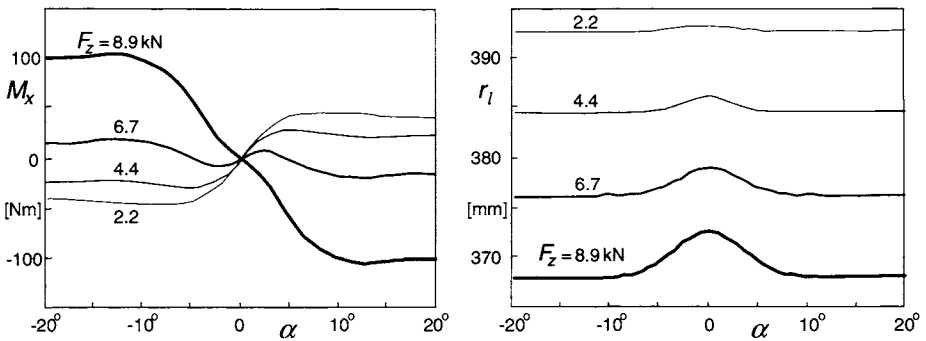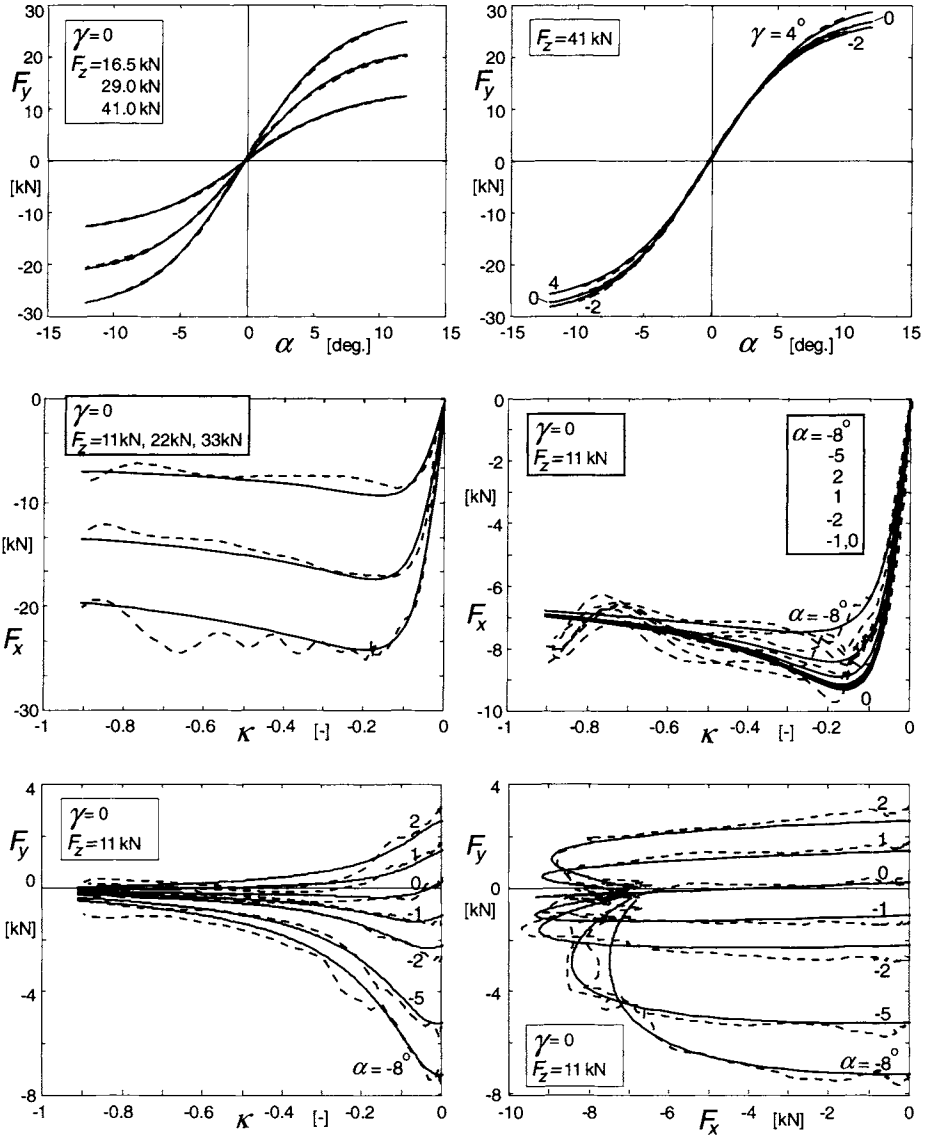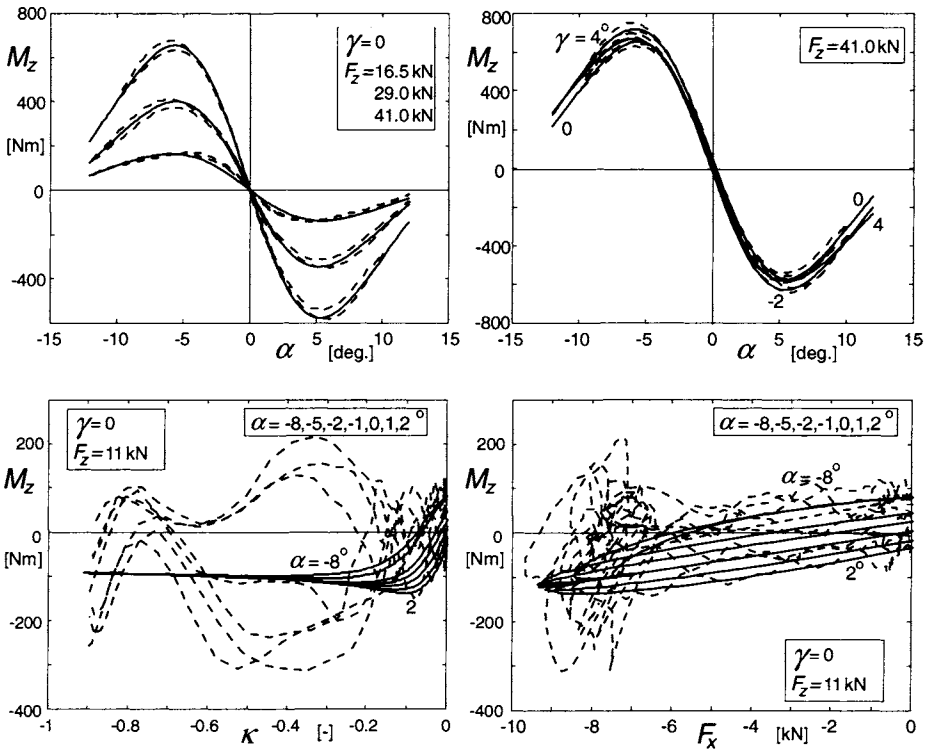
Fig. 4.29. Aligning torque characteristics of a 195/65 R15 car tyre. *Magic Formula* model
computed results compared with data from measurements (dotted curves) conducted
with the Delft Tyre Test Trailer (2000).

Fig. 4.30. Overturning couple and loaded radius of a passenger car tyre measured on Ford's
MTS Flat-Trac III tyre testing machine (V.d. Jagt 2000). Compare with Fig.4.26.

Fig. 4.31. Force characteristics of a 315/80 R22.5 truck tyre. *Magic Formula* computed results
compared with data from measurements conducted with the Calspan flat track tyre
test facility (2000) (dotted curves).

Fig. 4.32. Aligning torque characteristics of a 315/80 R22.5 truck tyre. *Magic Formula* computed results compared with data from measurements conducted with the Calspan flat track tyre test facility (2000) (dotted curves).

Exercise 4.1.   Assessment of off-nominal tyre side force characteristics and combined slip characteristics with F_x as input quantity

Consider the diagrams of Fig.4.33. For the original (nominal) side force characteristic $F_{yo}(\alpha)$ and for the cornering stiffness vs wheel load characteristic $C_{F\alpha}(F_z)$, employ the formulae as given by Eqs.(4.6-9) using the data indicated in the figure. The variation of camber stiffness with wheel load $C_{F\gamma}(F_z)$ is assumed to be linear. To cover the combined slip situation use Eqs.(4.41-44) (note: $C_{F\alpha}$ is expressed in N/degree, convert this first into N/rad to get in line with Eq.(4.42)). In Eq.(4.42a) choose $n = 4$. In the nominal condition we have parameter values:

$$F_{zo} = 3000\text{N}, \ \mu_o = 0.8, \ C_{F\alpha o} = 400\text{N/deg}, \ C_{F\gamma o} = 50\text{N/deg}.$$

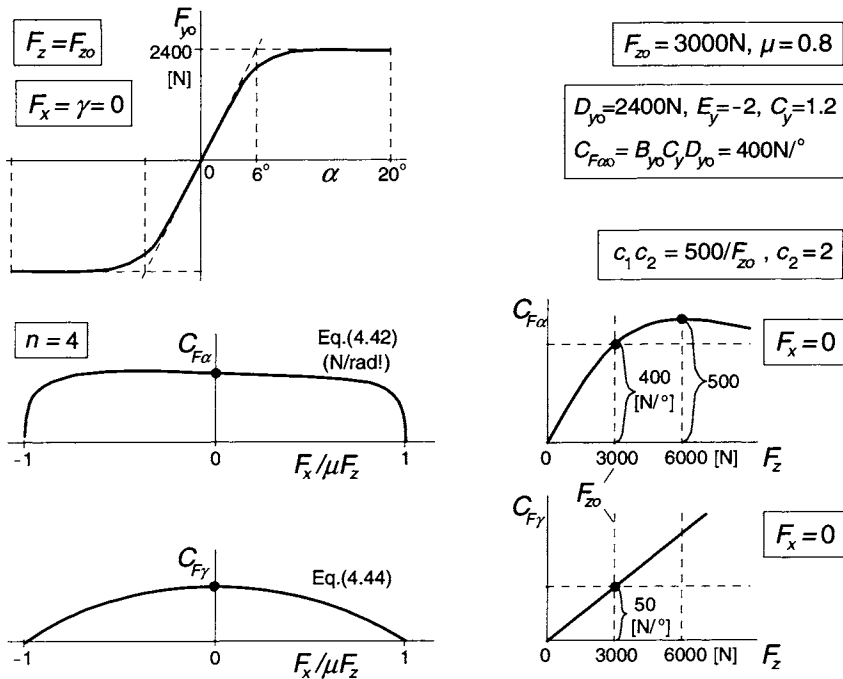Use Eqs.(4.45, 4.46) and do the following:

Fig. 4.33. On the assessment of off-nominal and combined slip tyre side force characteristics with longitudinal force as input quantity using the similarity method (Exercise 4.1).

1. Derive and plot the function $F_y(\alpha)$ for the following parameter values describing the tyre at a different condition:
   $F_z = 4000\text{N}$, $\mu = 0.9$, $\gamma = 4°$, $F_x = 2000\text{N}$.
2. Plot the graph for $F_y(F_x)$ for the constant slip angles $\alpha = 2$, 4, 6 and 8° at the condition $\mu = \mu_o$, $F_z = F_{zo}$ and $\gamma = 0$.

Exercise 4.2. Assessment of force and moment characteristics at pure and combined slip using the *Magic Formula* and the similarity method with κ as input

Given are the pure slip force and moment characteristics at nominal vertical load F_{zo} = 4000N and the cornering stiffness vs vertical load (cf. Figs.4.34a,b). The problems are formulated as follows:

1. Determine for the original curves, that is at the nominal load, the values of the coefficients B, C, D and E from the data indicated in the figures below. The vertical and horizontal shifts are disregarded. Use the formula (4.49) for the longitudinal force, the side force and also for the moment. Consider Fig.4.9 and use the formulae (4.52,4.53) and (4.56). Draw the resulting curves.
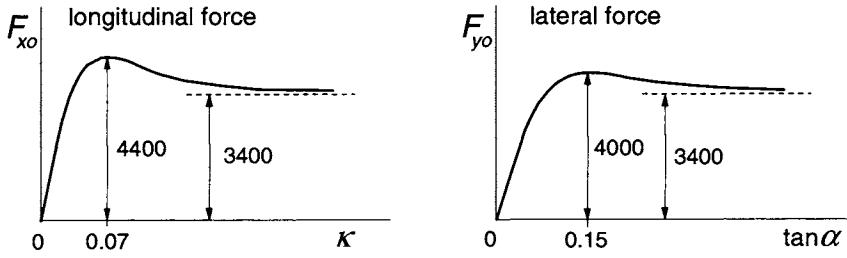
Fig. 4.34a. Original tyre force characteristics at pure slip (Exercise 4.2).

μ_{xo} $= 1.1$ μ_{yo} $= 1.0$

$F_{x,peak} = 4400\text{N}$ $F_{y,peak} = 4000\text{N}$

F_{xa} $= 3400\text{N}$ F_{ya} $= 3400\text{N}$

κ_m $= 0.07$ $\tan\alpha_m$ $= 0.15$

C_{Fko} $= C_{Fk}(4000)$ C_{Fao} $= C_{Fa}(4000)$
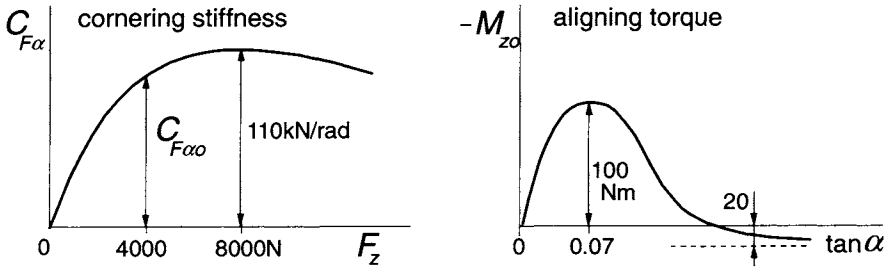
Fig. 4.34b. Cornering stiffness and original moment characteristics (Exercise 4.2).

p_1 $= 110\text{kN/rad}$ $-M_{z,peak} = 100\text{Nm}$

p_2 $= 8000\text{N}$ $-M_{za}$ $= -20\text{Nm}$

further: $\tan\alpha_m$ $= 0.07$

$C_{Fk}(F_z) = 40F_z$ [N] C_{Mao} $= C_{Ma}(4000)$

effective compliance parameter $t(F_z)$ $= 0.5\times10^{-5}\,F_z$ [m]

for M_z, Eq.(4.39): $C_{Ma}(F_z) = t.C_{Fa}(F_z)$ [Nm/rad]

c_9 $= 2\times10^{-5}\,F_{zo}/a_o$ c_{10} $= 0$

2. For $F_z = 2000$, 4000 and 6000N with $\mu_x = \mu_{xo}$ and $\mu_y = \mu_{yo}$ while $\gamma = 0$ compute and plot the curves for pure slip $F_x(\kappa)$, $F_y(\alpha)$ and $M_z(\alpha)$. Employ the similarity Eqs.(4.21-26).

3. For $F_z = 6000$N with $\mu_x = \mu_{xo}$, $\mu_y = \mu_{yo}$ and $\gamma = 0$ compute and plot the combined slip curves $F_y(F_x)$ and $M_z(F_x)$ at two slip angles: $\alpha = 2°$ and $8°$. The values of the longitudinal slip may range from $\kappa = -1$ to $+1$. Use Eqs.(4.27-29) and (4.35-40).